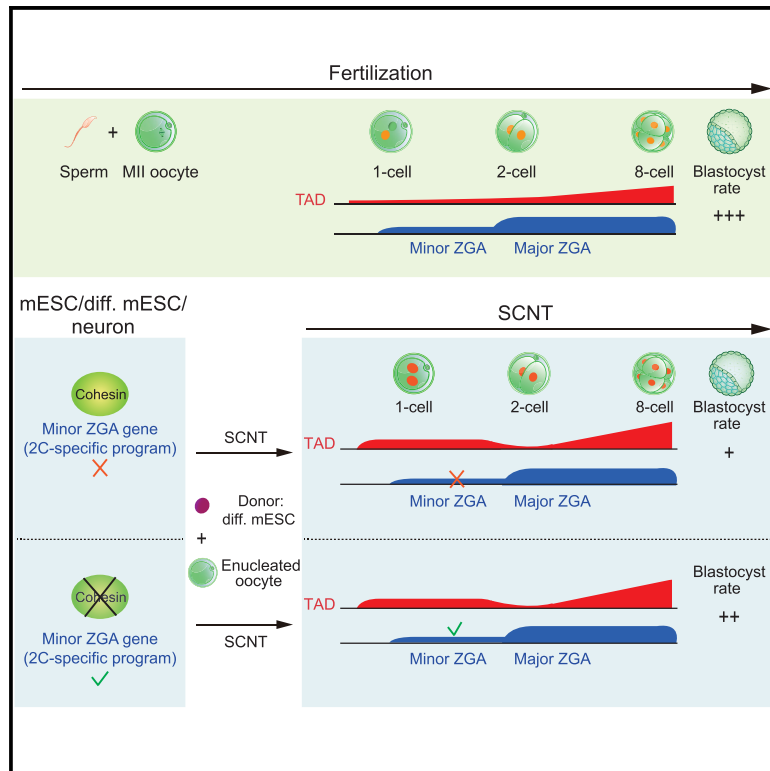# Analysis of Genome Architecture during SCNT Reveals a Role of Cohesin in Impeding Minor ZGA

Graphical Abstract

Authors

Ke Zhang, Dan-Ya Wu, Hui Zheng, ..., Robert J. Klose, Yi-Liang Miao, Wei Xie

Correspondence

miaoyl@mail.hzau.edu.cn (Y.M.), xiewei121@tsinghua.edu.cn (W.X.)

In Brief

Somatic cell nuclear transfer (SCNT) can reprogram a somatic nucleus to a totipotent state. By applying sisHi-C, Zhang et al. revealed a multi-step reprogramming of 3D chromatin architecture during SCNT. Surprisingly, they also found that pre-depleting cohesin in donor cells facilitates minor zygotic genome activation (ZGA) and SCNT.

Highlights

- Hi-C analysis of 3D chromatin architecture during somatic cell nuclear transfer (SCNT)

- TADs and compartments exhibit remarkable reprogramming during SCNT

- Cohesin represses minor ZGA genes in mESCs and differentiated cells

- Cohesin pre-depletion in donor cells facilitates minor ZGA and SCNT

CellPress

Article

Analysis of Genome Architecture during SCNT Reveals a Role of Cohesin in Impeding Minor ZGA

Ke Zhang,[1,6] Dan-Ya Wu,[2,3,6] Hui Zheng,[1,6] Yao Wang,[1,6] Qiao-Ran Sun,[2,3] Xin Liu,[2,3] Li-Yan Wang,[2,3] Wen-Jing Xiong,[2,3] Qiujun Wang,[1] James D.P. Rhodes,[4] Kai Xu,[1] Lijia Li,[1] Zili Lin,[1] Guang Yu,[1] Weikun Xia,[1] Bo Huang,[1] Zhenhai Du,[1] Yao Yao,[1] Kim A. Nasmyth,[5] Robert J. Klose,[5] Yi-Liang Miao,[2,3,*] and Wei Xie[1,7,*]

[1]Center for Stem Cell Biology and Regenerative Medicine, MOE Key Laboratory of Bioinformatics, School of Life Sciences, THU-PKU Center for Life Science, Tsinghua University, Beijing 100084, China
[2]Institute of Stem Cell and Regenerative Biology, College of Animal Science and Veterinary Medicine, Huazhong Agricultural University, Wuhan 430070, China
[3]Key Laboratory of Agricultural Animal Genetics, Breeding and Reproduction (Huazhong Agricultural University), Ministry of Education, Wuhan 430070, China
[4]MRC Laboratory of Molecular Biology, Cambridge, UK
[5]Department of Biochemistry, University of Oxford, Oxford, UK
[6]These authors contributed equally
[7]Lead Contact
*Correspondence: miaoyl@mail.hzau.edu.cn (Y.M.), xiewei121@tsinghua.edu.cn (W.X.)
https://doi.org/10.1016/j.molcel.2020.06.001

SUMMARY

Somatic cell nuclear transfer (SCNT) can reprogram a somatic nucleus to a totipotent state. However, the re-organization of 3D chromatin structure in this process remains poorly understood. Using low-input Hi-C, we revealed that, during SCNT, the transferred nucleus first enters a mitotic-like state (premature chromatin condensation). Unlike fertilized embryos, SCNT embryos show stronger topologically associating domains (TADs) at the 1-cell stage. TADs become weaker at the 2-cell stage, followed by gradual consolidation. Compartments A/B are markedly weak in 1-cell SCNT embryos and become increasingly strengthened afterward. By the 8-cell stage, somatic chromatin architecture is largely reset to embryonic patterns. Unexpectedly, we found cohesin represses minor zygotic genome activation (ZGA) genes (2-cell-specific genes) in pluripotent and differentiated cells, and pre-depleting cohesin in donor cells facilitates minor ZGA and SCNT. These data reveal multi-step reprogramming of 3D chromatin architecture during SCNT and support dual roles of cohesin in TAD formation and minor ZGA repression.

INTRODUCTION

In eukaryotes, the genome is not in the linear state but is instead packaged into highly organized chromatin fibers (Bickmore, 2013; Gibcus and Dekker, 2013; Gorkin et al., 2014). Proper higher-order chromatin folding is crucial for gene regulation and chromosome division during mitosis or meiosis (Gibcus and Dekker, 2013; MacGregor et al., 2019; Zheng and Xie, 2019). Investigations using various 3D genome technologies, including chromosome conformation capture based on proximity ligation ("C technologies") and microscopy imaging, have revealed multi-layer high-order chromatin configuration (Gibcus and Dekker, 2013). In mammals, the genome is partitioned into megabase-size compartments (such as A or B) that correlate with the transcription activity and gene density (Lieberman-Aiden et al., 2009). At often sub-megabase scales, topologically associating domains (TADs) exist as contact domains independent of compartments A/B (Rowley and Corces, 2016). These TADs likely arise via loop extrusion, as cohesin extrudes chro-matin until it is blocked by CTCF or other cis-acting factors (Davidson et al., 2019; Fudenberg et al., 2016; Kim et al., 2019; Nasmyth and Haering, 2009; Rowley and Corces, 2016). Finally, at even finer scale, the interactions among regulatory elements, such as promoters and enhancers, are crucial in regulating appropriate gene expression (Gorkin et al., 2014; Pombo and Dillon, 2015).

Notably, chromatin architecture undergoes drastic re-organization during early embryogenesis. In mouse, sperm displays conventional TADs and compartmentalization (Battulin et al., 2015; Du et al., 2017; Jung et al., 2017; Ke et al., 2017). Mature oocytes, which are arrested at the metaphase II stage, show a mitotic-chromatin-like organization that is virtually depleted of TADs and chromatin compartments (Du et al., 2017; Ke et al., 2017). However, after fertilization, chromatin adopts a highly dispersed or relaxed state at the 1-cell stage, as revealed by electron spectroscope imaging (Ahmed et al., 2010) and Hi-C (Collombet et al., 2020; Du et al., 2017; Ke et al., 2017), with the strengths of both TADs and compartments strongly reduced.
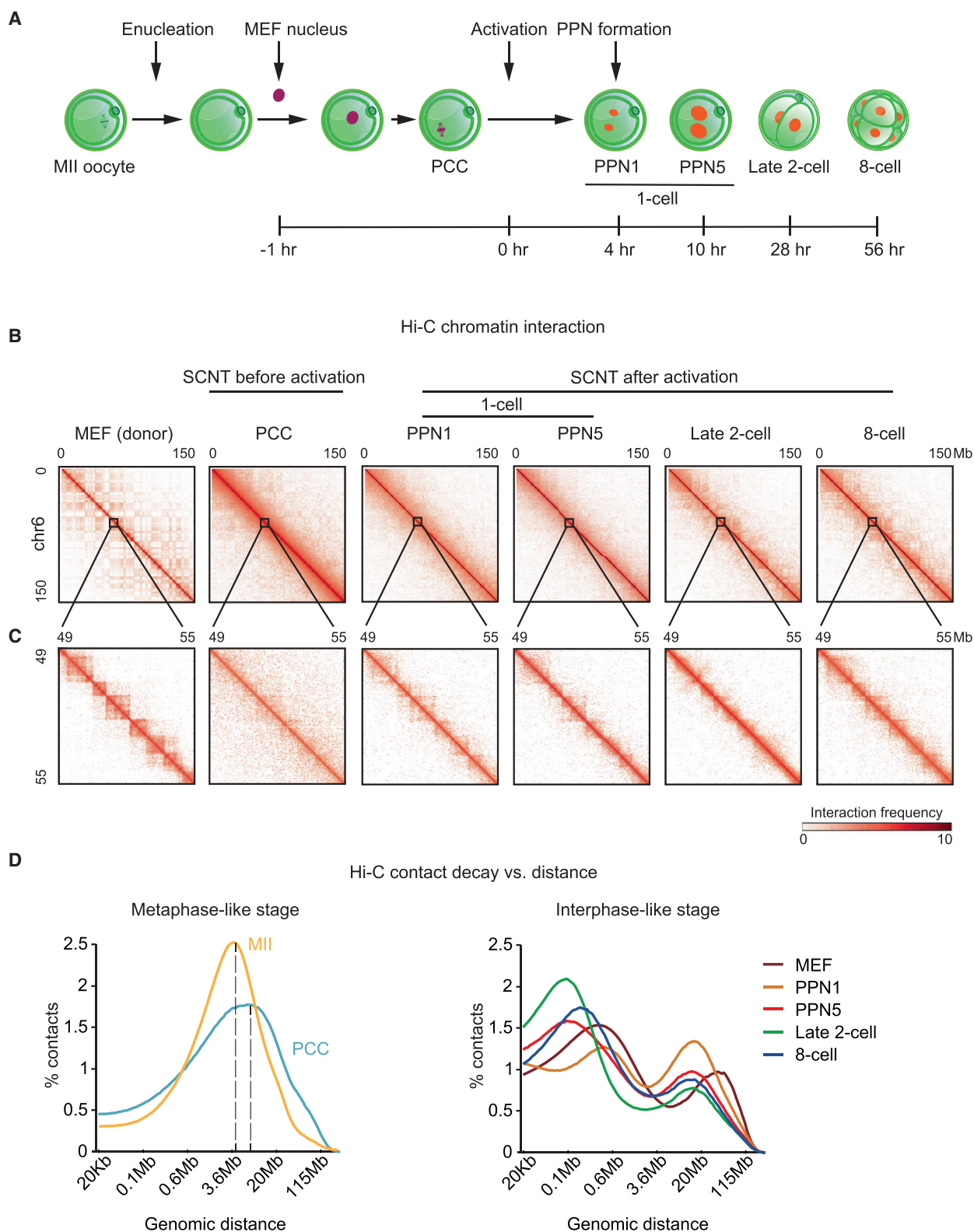
Figure 1. Mapping 3D Genome Organization Transitions during SCNT

(A) Schematic of the SCNT process. MEF donor nuclear was transferred into enucleated MII oocyte. The SCNT embryo then transited to the PCC stage (premature chromosome condensation) (1 h after nuclear transfer). The exit of PCC stage was induced through SCNT activation using strontium chloride (SrCl$_2$).

(legend continued on next page)

Nevertheless, weak TADs and loops can still be detected in zygotes and are also cohesin dependent (Flyamer et al., 2017; Gassler et al., 2017). During early embryogenesis, the re-establishment of chromatin structure is unusually slow, and the consolidation of TAD and chromatin compartmentalization is not completed until the 8-cell stage. Remarkably, such relaxed chromatin organization at early stages was also observed in fly (Hug et al., 2017), fish (Kaaij et al., 2018; Nakamura et al., 2018), and human (Chen et al., 2019), suggesting that this is an evolutionarily conserved feature of early embryos. However, how this occurs and whether it regulates early development remain a mystery.

Somatic cell nuclear transfer (SCNT) technology can reprogram somatic cells to a totipotent embryo and produce viable offspring (Gurdon, 2006). This process is accompanied by dramatic chromatin re-organization induced by ooplasm. After the introduction into the enucleated MII oocyte, the somatic nucleus folds into a premature chromatin condensation (PCC) state by adopting metaphase-like rod morphology, likely driven by the high level of maturation-promoting factors (or mitosis-promoting factors [MPFs]) in oocyte cytoplasm (Campbell et al., 1996). The SCNT embryos can be "activated" through chemical or electrical signals, leading to the inactivation MPF through degradation of cyclin B and PCC exit. This is followed by the segregation of donor chromosomes to form a pronuclei-like structure (pseudo-pronuclei; Wakayama et al., 1998). The subsequent development shares many features with fertilized embryos. For example, the zygotic genome activation (ZGA) of mouse SCNT embryos initiates around the similar time as fertilized embryos—the 2-cell stage (Matoba and Zhang, 2018). Nevertheless, compared to natural fertilization, SCNT usually shows markedly low development efficiency, likely due to incomplete epigenetic reprogramming. For example, the addition of KDM4D or KDM4B, the histone demethylase of H3K9me3, or the histone deacetylase inhibitors, can significantly promote SCNT efficiency (Kishigami et al., 2006; Liu et al., 2016; Matoba et al., 2014; Rybouchkin et al., 2006). Notably, these reagents are known to facilitate chromatin de-compaction (Allis and Jenuwein, 2016; Grunstein, 1997; Kretsovali et al., 2012). Nevertheless, most SCNT embryos still cannot survive to term (Matoba and Zhang, 2018), implying that critical epigenetic defects are yet to be identified. To date, how chromatin is reprogrammed at the molecular level during SCNT, especially for the 3D chromatin architecture, remains poorly understood. In this study, we systematically probed the dynamics of 3D chromatin architecture during the mouse SCNT embryogenesis. Our results revealed that chromatin structure undergoes de-compaction and stepwise re-organization during the SCNT embryogenesis. Importantly, we showed that pre-depleting cohesin in donor cells facilitates SCNT development, in part through promoting minor zygotic genome activation.

RESULTS

Drastic 3D Chromatin Re-organization during SCNT Development

To examine the dynamics of global chromatin architecture during the transition from somatic cells to totipotent embryos, we first collected donor mouse embryonic fibroblast (MEF) cells, the SCNT embryos at the PCC stage (premature chromosome condensation), and SCNT embryos after PCC exit (through "activation" using strontium chloride [$SrCl_2$]) at the 1-cell, late 2-cell, and 8-cell stages. For comparison, we considered SCNT PCC embryos before activation to be similar as MII oocytes before sperm fertilization (see below) and 1-cell SCNT embryos after activation to be similar to fertilized 1-cell zygotes. For SCNT 1-cell embryos, we collected embryos at two time points, including PPN1 (pseudo-pronucleus stage 1) (representing early 1-cell) and PPN5 (pseudo-pronucleus stage 5) (representing late 1-cell; STAR Methods; Figures 1A, S1A, and S1B). We then applied low-input in situ Hi-C (sisHi-C) (Du et al., 2017) to these samples (Table S1) and confirmed their reproducibilities between replicates (Figure S1C). Next, we investigated the dynamics of global chromatin interaction during SCNT development (Figures 1B and 1C). The SCNT-PCC embryos show relatively fewer inter-chromosomal read pairs (Figure S1D). The global contact decay curve of the SCNT-PCC embryos also resembles that of metaphase chromatin, with a single peak (~5 Mb) that presumably represents an interaction boundary along the axis of the mitotic chromatin (Figure 1D; Du et al., 2017; Flyamer et al., 2017; Gibcus et al., 2018; Ke et al., 2017; Nagano et al., 2017; Naumova et al., 2013). These data are in line with the notion that chromatin is rapidly condensed by MPFs in the ooplasm, a process that facilitates genome silencing to allow the successful somatic-to-embryonic transition (Campbell et al., 1996; Kim et al., 2002; Wakayama et al., 1998). By contrast, the interaction decay plot shows two peaks in post-activation SCNT embryos and MEFs (Figure 1D) that are characteristic of interphase cells.

Next, we investigated the dynamics of TADs during SCNT development. Interestingly, compared to those in MEFs, TADs become markedly weak, although still visible, in PCC SCNT embryos (Figures 1C and S2A). As a comparison, TADs are virtually absent in metaphase cell or MII oocytes (Du et al., 2017; Flyamer et al., 2017; Gibcus et al., 2018; Ke et al., 2017; Nagano et al., 2017; Naumova et al., 2013). Although the residual TADs may reflect different chromatin folding mechanisms between SCNT-PCC embryos and MII oocytes, it is also possible that they are caused by the asynchronized nature of PCC embryos, as only 85% of the collected embryos show rod-like condensed chromatin (Figure S2B). Nevertheless, TADs become even slightly stronger in 1-cell SCNT-PPN embryos (Figures 1C and S2A). This is in contrast to their counterpart of fertilized 1-cell embryos,
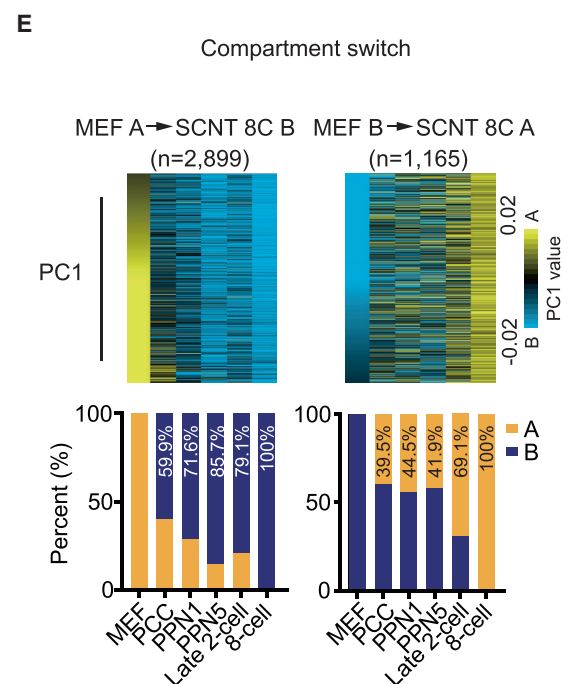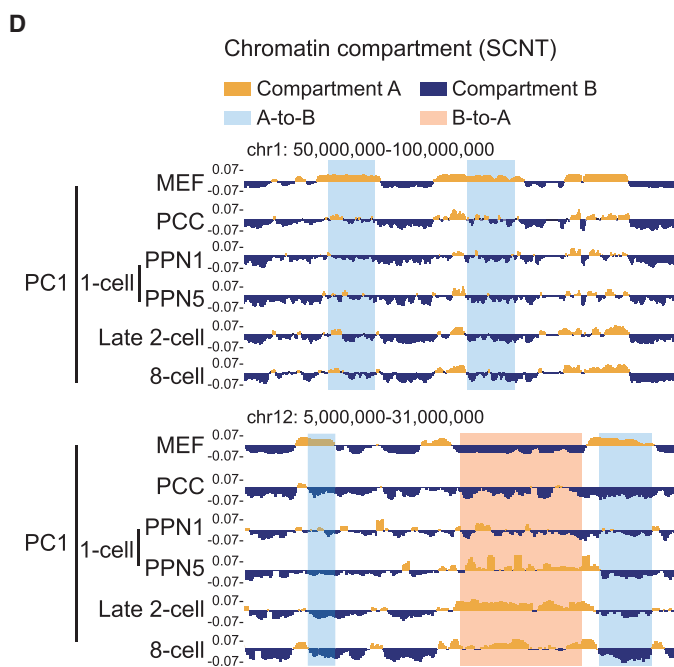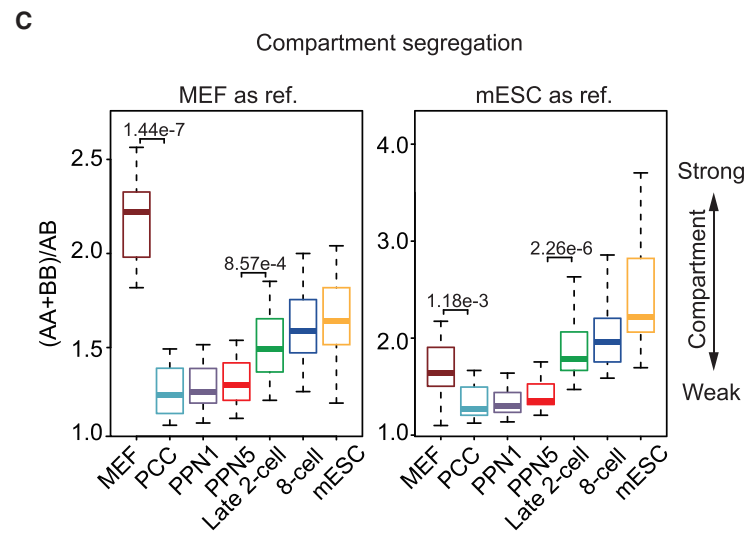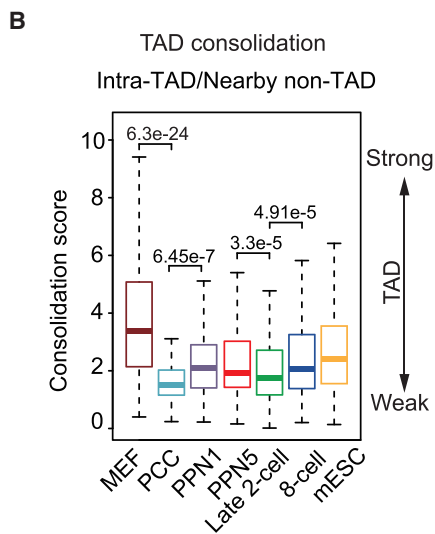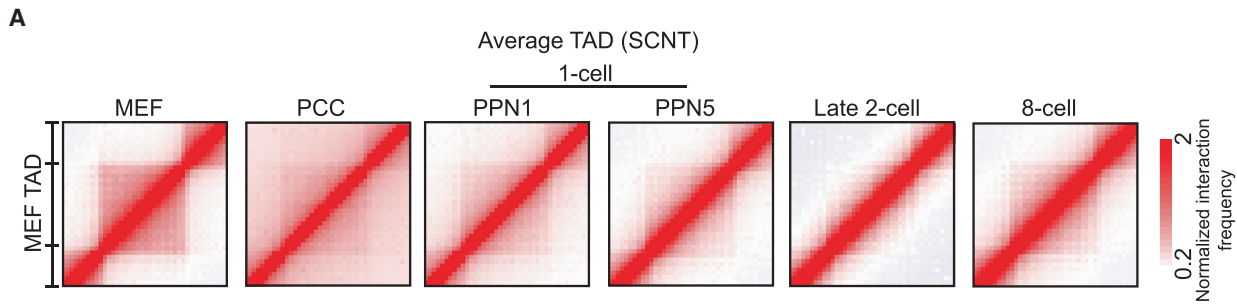

SCNT 1-cell embryos include early 1-cell embryos (4 h after activation; PPN1 [pseudo-pronucleus stage 1]) and late 1-cell embryos (10 h after activation; PPN5 [pseudo-pronucleus stage 5]). SCNT embryos at late 2-cell (28 h after activation) and 8-cell (56 h after activation) stages were also collected.
(B) Heatmaps showing the normalized Hi-C interaction frequencies (300-kb bin, chr6) before or after $SrCl_2$ activation.
(C) Zoomed-in views (40-kb bin) are also shown (pooled data from 2 biological replicates).
(D) Contact decay profile of each cell type was calculated as previously described (Nagano et al., 2017; STAR Methods). Left: metaphase-like stages with only one peak, including PCC and MII oocyte, are shown. Right: interphase-like stages with two peaks, including MEF and SCNT embryos, are shown.
See also Figure S1 and Table S1.

A Average TAD (SCNT)

MEF | PCC | PPN1 | PPN5 | Late 2-cell | 8-cell

B TAD consolidation
Intra-TAD/Nearby non-TAD

C Compartment segregation
MEF as ref. | mESC as ref.

D Chromatin compartment (SCNT)

chr1: 50,000,000-100,000,000

chr12: 5,000,000-31,000,000

E Compartment switch

MEF A → SCNT 8C B (n=2,899) | MEF B → SCNT 8C A (n=1,165)

which have much weaker TADs (Du et al., 2017; Ke et al., 2017). Intriguingly, TADs become diminished in late 2-cell SCNT embryos, before they are strengthened again at the 8-cell stage (Figures 1C and S2A), as confirmed by the overall TAD strengths (using TADs defined in MEF; Figures 2A and S2C; STAR Methods), TAD consolidation (Du et al., 2017; Figures 2B and S2D), and boundary insulation (Crane et al., 2015; Figure S2E). We then examined the states of chromatin compartmentaliza-tion. Although compartments A and B (the "checkerboard pat-terns" in the interaction heatmaps) are clearly visible in MEFs, they are significantly weakened in SCNT-PCC embryos (Fig-ure S2F). Unlike TADs, compartments remain weak at the 1-cell PPN stage and only become strengthened at the late 2-cell stage and onward (Figures 2C and S2F). Despite their weak strengths, we identified compartments through the prin-cipal-component analyses (PCA) at each stage and asked when they transit from donor cells to embryos (Figure 2D). By the late 1-cell stage (PPN5), a large portion (85.7%) of MEF-spe-cific compartment A (compared to SCNT 8-cell embryos) already becomes B compartment (Figures 2D and 2E). As a comparison, a smaller fraction (41.9%) of MEF-specific compartment B switches to compartment A. The percentage increases to 69.1% at the late 2-cell stage (Figures 2D and 2E). The relatively slower kinetics of B-to-A switch perhaps reflects the resistance of reprogramming by gene deserts and heterochromatin (Ma-toba et al., 2014). Thus, these data indicate that the somatic-to-embryonic compartment switch occurs as early as the early 1-cell stage (PPN1). This result also echoes the finding that the global chromatin accessibility (revealed by DNase-seq [DNase I hypersensitive site sequencing] analysis) is reset at the 1-cell stage in SCNT embryos (Djekidel et al., 2018). Hence, these data reveal multi-step reprogramming of chromatin architecture during SCNT embryo development.

Comparison of TAD and Compartment Dynamics between SCNT and Fertilized Embryos

We then compared the reprogramming of chromatin architecture in SCNT embryos to that of fertilized embryos (Du et al., 2017). TADs in SCNT 1-cell (PPN) embryos are clearly stronger than those in fertilized 1-cell embryos, as confirmed by global average TADs and differential interaction analyses (Figures 3A and S3A). Previously, we also observed weak TADs in fertilized middle 1-cell embryos (PN3 stage; Du et al., 2017). Hence, we conduct-

ed Hi-C in middle 1-cell SCNT embryos (PPN3; pseudo-pronu-cleus stage 3; STAR Methods), which again showed relatively stronger TADs in SCNT embryos (Figure 3A). The strengths of TADs then become similar between SCNT and fertilized embryos at the late 2-cell stage (Figures 3A, 3B, S3B, and S3C), before both further increase at the 8-cell stage. Hence, TAD relaxation also occurs in SCNT embryos but at a later stage (2-cell) compared to that in fertilized embryos (1-cell), implying that perhaps chromatin relaxation is less efficient or delayed for SCNT embryos.

Next, we asked how chromatin architecture at individual loci is reprogrammed in SCNT compared to that of fertilized embryos. As high-depth Hi-C data are required for fine-resolution analysis of TADs, we could not identify reliable TAD positions directly in SCNT embryos (data not shown). Therefore, we used pooled TAD boundaries in MEFs and mouse embryonic stem cells (mESCs) (the sample closest to embryos where deep Hi-C data are available) and further refined the precise boundary po-sitions using the CTCF binding sites within the TAD boundary bins (n = 6,979). We then defined "TAD boundary strength" (TBS) as the Hi-C insulation score differences between the CTCF binding site and its neighbor regions ($\pm$120 kb; Figure 4A; STAR Methods). Next, we identified "dynamic TAD boundaries" with significantly different TBS scores between fertilized 8-cell embryos and MEF (ΔTBS > 0.7) and further required the TAD boundary to be lost in one of the two cell types. The rest TAD boundaries were considered as "static." Dynamic TAD bound-aries were further classified as "reprogrammed," "resistant," or "intermediate," depending on whether $TBS_{(SCNT)}$ is closer to $TBS_{(Fertilized)}$ or $TBS_{(MEF)}$ (STAR Methods). In total, about 7.8% (540 out of 6,979) TAD boundaries were defined as reprog-rammed and 3.8% were considered as resistant (Figure 4B). The same analysis on each replicate separately (instead of the pooled samples) confirmed that the reprogrammed and resistant TAD boundaries are reproducible (Figures S4A–S4C), and only those identified by both replicates were used for downstream analysis. We hypothesized that, if a TAD boundary is resistant to reprogramming, it may cause mis-regulation of gene expres-sion near these boundaries in SCNT embryos. By identifying differentially expressed genes (DEGs) between SCNT 8-cell and fertilized 8-cell embryos (Zheng et al., 2016), we found that resistant TAD boundaries indeed preferentially reside near DEGs, as also confirmed by an analysis of DEG using each

Figure 2. Drastic Chromatin Re-organization during SCNT Embryo Development
(A) Heatmaps showing the normalized average interaction frequencies for all TADs (defined in MEF) as well as their nearby regions ($\pm$0.5 TAD length) at different SCNT stages (replicates pooled; n = 2).
(B) Boxplots showing the consolidation scores (intra-TAD interactions/neighbor non-TAD interactions; Du et al., 2017) at different SCNT stages. p values calculated by Wilcoxon rank-sum test (two-tailed) are also shown.
(C) Boxplots showing segregation levels for compartments. Segregation strengths were calculated as interaction ratios defined by (AA + BB)/(AB). MEF com-partments (left) or mESC compartments (right) were used as references to represent conventional compartments. p values calculated by Wilcoxon rank-sum test (two-tailed) are also shown.
(D) The UCSC genome browser views showing chromatin compartments (principal component 1 values or PC1 values; STAR Methods; pooled data from 2 biological replicates). Positive and negative PC1 values represent compartment A (yellow) and B (blue), respectively. Regions with A-to-B or B-to-A compartment switches are shaded (100-kb bin resolution).
(E) Top: heatmaps showing the dynamics of PC1 values for different SCNT stages in MEF-specific compartment A (yellow) or B (blue; compared to the SCNT 8-cell embryos). Bottom: bar charts show percentages of compartments A and B based on bin numbers (bin size = 100 kb) at various developmental stages for either MEF-specific compartment A or MEF-specific compartment B categories. The percentage numbers are also shown.
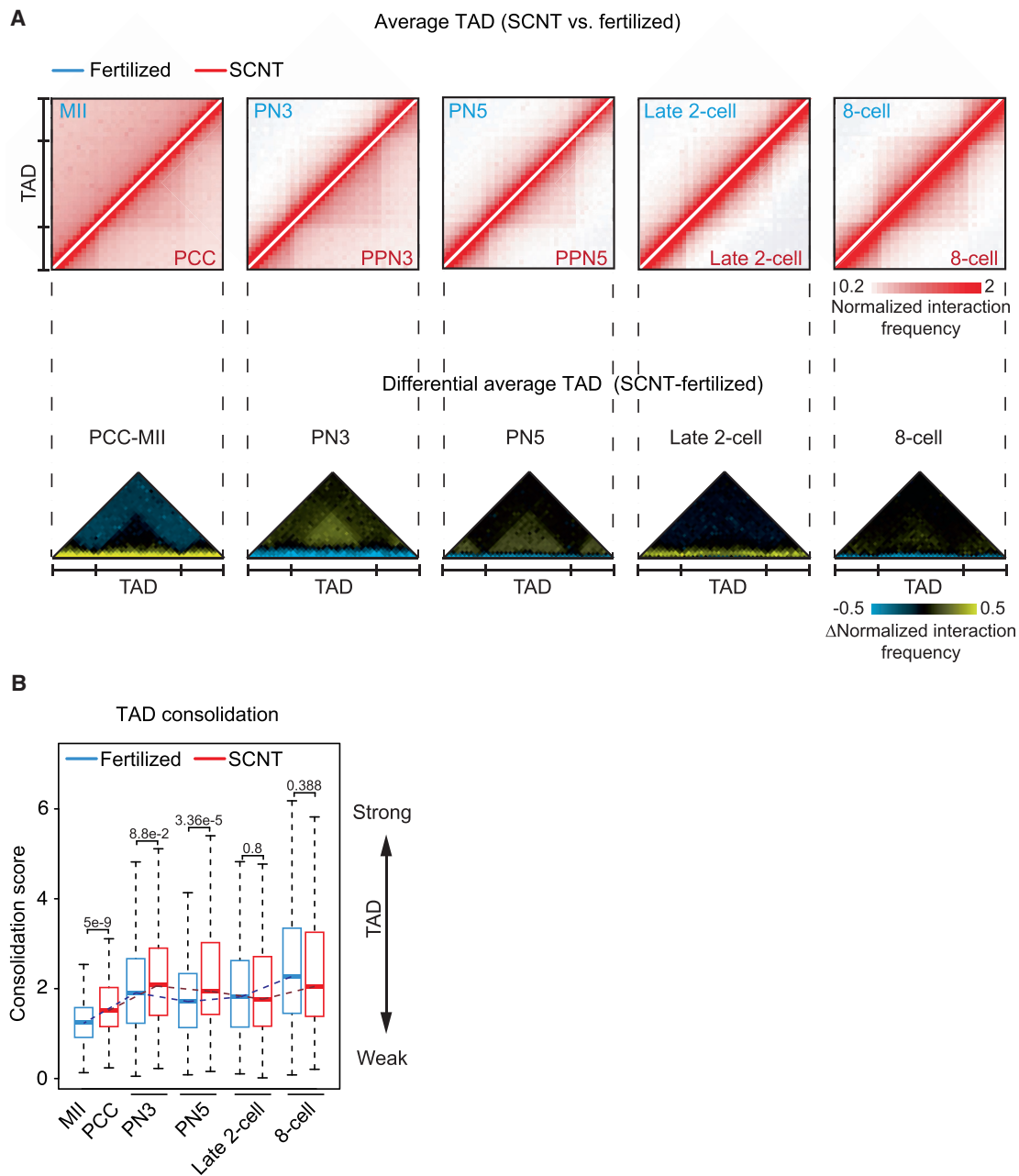See also Figure S2.

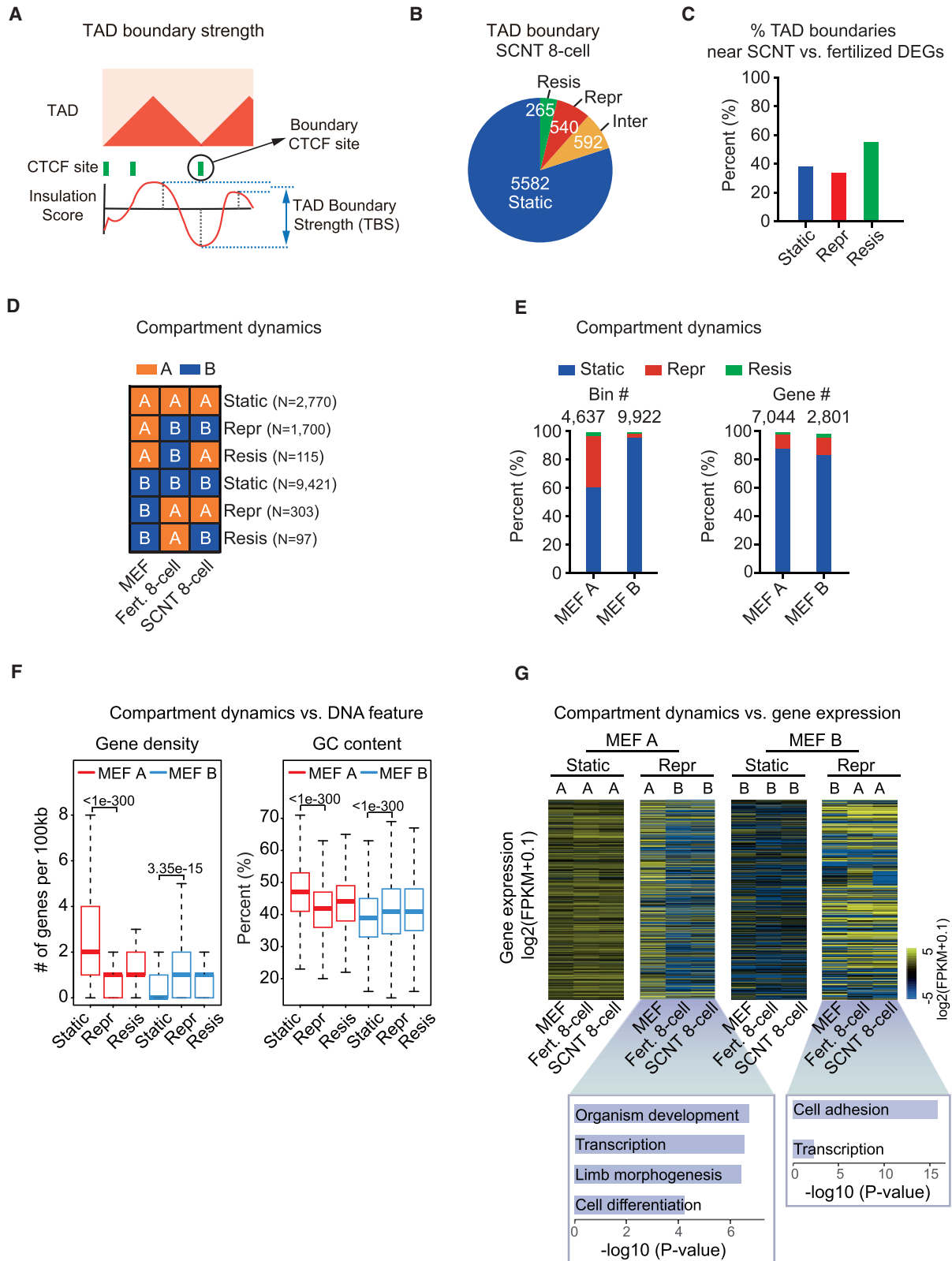**Figure 3. Comparison of TAD Dynamics between SCNT Embryos and Fertilized Embryos**
(A) Top: heatmaps of normalized average interaction frequencies for all TADs as well as their nearby regions (±0.5 TAD length) at various developmental stages for fertilized embryos (Du et al., 2017; top left) and SCNT embryos (bottom right; replicates pooled; n = 2). For SCNT embryos, MEF TAD locations were used; for fertilized embryos, ICM TAD locations were used. Similar results were also obtained by both using MEF TAD locations (data not shown). Bottom: differential heatmaps showing the differences for normalized TAD strengths between SCNT and fertilized embryos at various stages.
(B) Boxplots showing the consolidation scores for fertilized (Du et al., 2017) or SCNT embryos at various stages (replicates pooled; n = 2). The dashed lines show the average TAD consolidation scores among stages. p values calculated by Wilcoxon rank-sum test (two-tailed) are also shown.
See also Figure S3.

individual replicate of RNA sequencing (RNA-seq) (Figures 4C and S4D). Interestingly, DEGs near resistant TAD boundaries, despite their small numbers (n = 32), were enriched for those involved in "embryonic development" (p value = 1.7E−2), such as *Sod1*, *Eng*, *Mfap2*, and *Jak2* (Figure S4E). For example,

ENG (endoglin), which is downregulated in SCNT embryos, is a transforming growth factor β (TGF-β) receptor, and TGF-β family is known to be essential for embryonic development (Wu and Hill, 2009). JAK2, which is upregulated in SCNT embryos, is a tyrosine kinase and plays an important role in the early lineage

A TAD boundary strength

B TAD boundary SCNT 8-cell

C % TAD boundaries near SCNT vs. fertilized DEGs

D Compartment dynamics

E Compartment dynamics

F Compartment dynamics vs. DNA feature

G Compartment dynamics vs. gene expression

(legend on next page)

decision of mESC differentiation and embryonic hematopoiesis (Chung et al., 2006). Taken together, these data suggest that TAD boundaries undergo dynamic reprogramming during SCNT, and those that fail to be reprogrammed are preferentially associated with mis-regulated genes.

We then asked how chromatin compartmentalization is reprogrammed during SCNT compared to that in fertilized embryos. Similarly, we classified all MEF compartments into three groups based on whether they switch compartments in fertilized embryos and SCNT embryos (Figure 4D). These include (1) static compartments, defined as those that remain A or B in all three cell types (MEF, fertilized 8-cell, and SCNT 8-cell embryos); (2) reprogrammed, defined as those that are A in MEF but become B in both fertilized and SCNT 8-cell embryos (or vice versa); and (3) resistant, referring to those that switch compartments in fertilized embryos but fail to do so in SCNT embryos. Genome-widely, 59.7% and 95.0% of compartments A and B in MEF are classified as static (Figure 4E). About 36% of A in MEF switch to B in both fertilized embryos and SCNT (reprogrammed; Figure 4E). As a result, static and reprogrammed regions together occupy 97.5% and 99.0% compartments A and B in MEF, respectively, suggesting that most compartments are correctly reprogrammed in SCNT embryos. Notably, "static A" and "static B" compartments have the highest and lowest gene densities and guanine-cytosine (GC) contents, respectively (Figure 4F). By contrast, reprogrammed and resistant compartments show intermediate gene densities and GC contents (Figure 4F). Importantly, genes in reprogrammed MEF compartments display correlated transcriptional changes in both fertilized and SCNT 8-cell embryos (Figure 4G). These genes are primarily involved in organism development, transcription, embryonic limb morphogenesis, and cell differentiation (Figure 4G). To ask whether such compartment dynamics is true for SCNT using different donor cells, we used cumulus cells (CC) as alternative donor cells and repeated Hi-C analyses for them and the derived 8-cell SCNT embryos (Figure S5A). Consistently, most compartment B (94.7%) in cumulus cells fall in the static class and 23.9% of compartment A is reprogrammed to B during SCNT (Figures S5B and S5C). Interestingly, the cell-type-specific compartments between MEF and cumulus cells (MEF-A/CC-B or MEF-B/CC-A) both preferentially become compartment B in SCNT embryos (Figures S5D–S5F), indicating silencing of somatic-

cell-specific programs during SCNT. Finally, we also identified a very small set of resistant compartment regions (2.48% compartment A and 1.0% compartment B of MEF; Figures 4D and 4E), which failed to switch to the fertilized embryo compartments. Unexpectedly, the expression of genes in these compartments still switched to a pattern that resembles that of fertilized 8-cell embryos (Figure S6A; see examples in Figure S6B). Consistently, these resistant compartments also do not overlap with previous "reprogramming resistant regions (RRRs)" identified by RNA-seq (Matoba et al., 2014; Figure S6C). Although such small sets of compartments may reflect false compartment calling, it is also known that the expression changes of individual genes do not always correlate with changes of compartments (Quinodoz et al., 2018). It is possible that robust transcriptional regulatory network may exist to ensure the proper gene expression reprogramming during SCNT despite the inappropriate compartments. Taken together, these data suggest that both TAD and compartment undergo efficient reprogramming toward "fertilized patterns" during SCNT development, despite a small set of resistant regions.

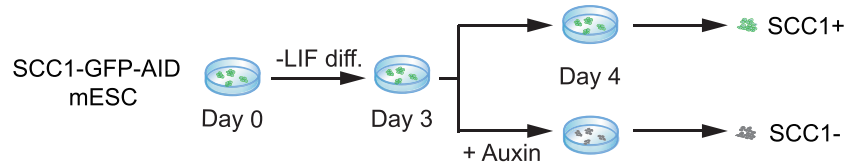## Pre-depletion of Cohesin from Donor Cells Improves SCNT Efficiency

The fact that TADs of SCNT embryos at 1-cell stage are much stronger than that of the fertilized counterparts raises interesting questions as to (1) whether the defective or delayed chromatin relaxation in SCNT embryos reflects inefficient chromatin reprogramming and (2), if so, whether such inefficient reprogramming may impede SCNT embryogenesis. Therefore, we sought to promote the relaxation of donor chromatin by removing cohesin, the architectural protein complex that is essential for loop and TAD formation (Haarhuis et al., 2017; Rao et al., 2017; Schwarzer et al., 2017). Because cohesin is also crucial for the cell survival (Nasmyth and Haering, 2009), we used a mESC line that employs the auxin-induced degron (AID) to acutely deplete SCC1 (Rhodes et al., 2020), a key subunit of cohesin (Nasmyth and Haering, 2009; Figure 5A). To mimic the somatic chromatin state, we first differentiated these mESCs by withdrawing LIF (leukemia inhibitory factor) for 3 days (Figure S6D) and then applied auxin treatment for 1 day (Figures 5A and S6E). Hi-C analysis confirmed the decrease of TAD strengths and boundary insulation (Figure 5B).

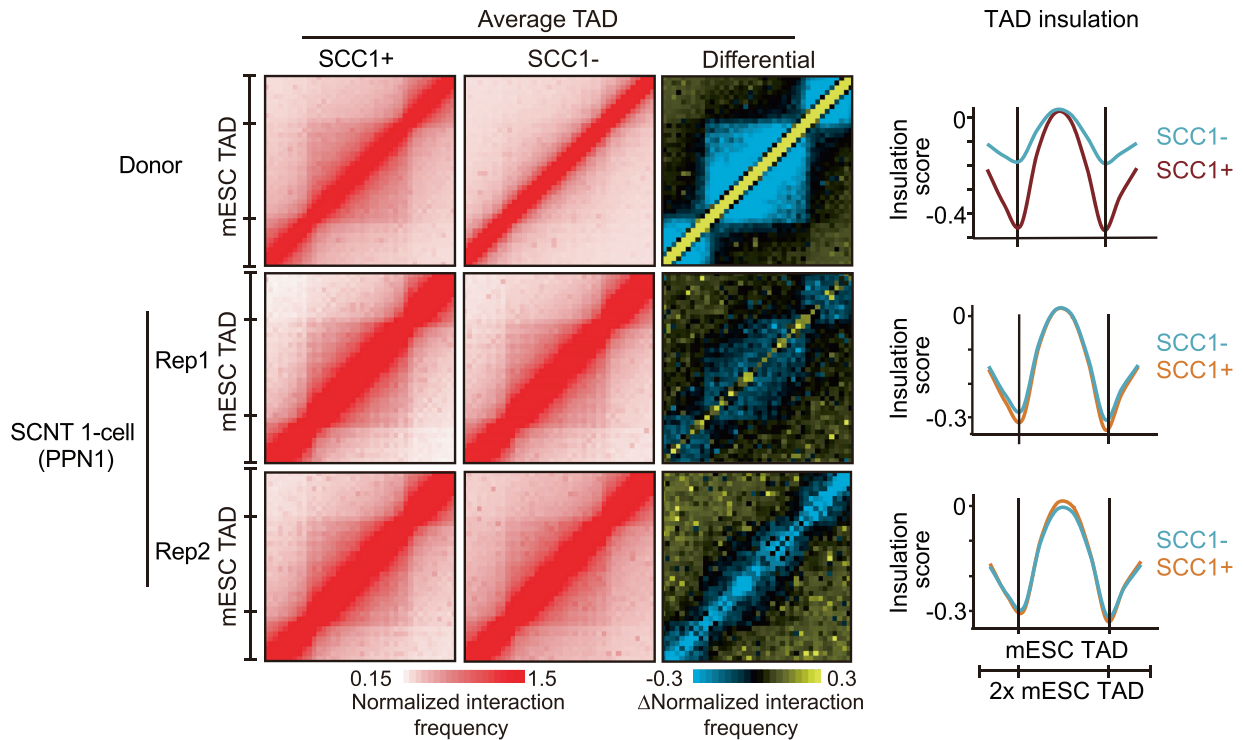**Figure 4. Reprogramming of TAD and Compartment during SCNT Development**

(A) Schematic shows the method to compute TAD boundary strength (TBS), which equals to the average insulation score differences between TAD boundaries (CTCF sites) and their nearby regions (±120 kb; 3 bins in Hi-C matrix).

(B) Pie charts showing the percentages of "static," "intermediate (Inter)," "reprogrammed (Repr)," and "resistant (Resis)" TAD boundaries (STAR Methods).

(C) Bar charts showing the percentages of TAD boundaries in each boundary group residing near 8-cell fertilized-SCNT DEGs (within 1 Mb). DEGs were identified using 3 RNA-seq replicates combined (fold change > 5; either SCNT or fertilized 8-cell embryos show minimal FPKM of 5).

(D) Table showing the classification of chromatin compartments (STAR Methods). The numbers of bins (bin size = 100 kb) in each compartment class are listed.

(E) Bar charts showing the percentages of bin numbers (bin size = 100 kb) for each class among MEF compartment A/B regions (left). The corresponding genes falling into these compartments for each class are also shown similarly (right). The total numbers of bins (bin size = 100 kb) or genes are shown above the bar charts.

(F) Left: boxplots showing the gene densities (left) or GC content (right) in each class (with MEF compartment A/B regions separated). p values calculated by Wilcoxon rank-sum test (two-tailed) are also shown.

(G) Heatmaps showing the gene expression levels for each class in donor MEF and fertilized 8-cell and SCNT 8-cell embryos. MEF compartments A (left) and B (right) are separately analyzed. Gene expression data were quantile normalized among different cell types. GO analysis for Repr (reprogrammed) class is also shown.

See also Figures S4–S6.

A

B

Average TAD | TAD insulation

0.15 ▮ 1.5
Normalized interaction
frequency

-0.3 ▮ 0.3
ΔNormalized interaction
frequency

C

SCNT developmental efficiency

SCC1+
(3 rep, n=192)

SCC1-
(3 rep, n=177)

D
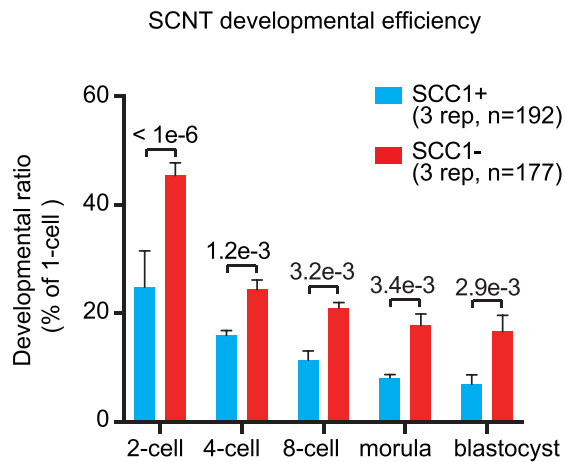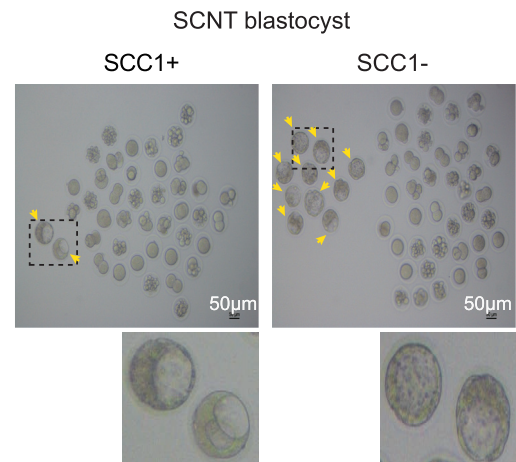
SCNT blastocyst

SCC1+   SCC1-

50μm   50μm

(legend on next page)

We then conducted SCNT experiments using these cohesin pre-depleted nuclei. It is worth noting that there was no auxin during SCNT; therefore, the re-expression of cohesin in early embryos is expected to be unaffected. Strikingly, SCNT embryos derived from cohesin-depleted donor nuclei showed increased blastocyst rates (Figure 5C). Such improvement in embryo development is surprising given that cohesin is typically required for cell viability. To test whether cohesin pre-depletion may promote SCNT through relaxing TADs in 1-cell SCNT embryos, we performed sisHi-C in SCNT 1-cell embryos (PPN1 stage) derived from SCC1 pre-depleted donor cells. Unexpectedly, although TADs are lost in donor cells upon SCC1 depletion, they are rapidly restored in 1-cell SCNT embryos after nuclear transfer (Figure 5B), suggesting that the lack of auxin during SCNT (for about 10 h from nuclear transfer to PPN1 stage) quickly relieved SCC1 from auxin-induced degradation. Thus, we concluded that pre-depletion of cohesin in donor cells significantly promotes SCNT development, despite the persisting global TADs in 1-cell embryos.

Cohesin Pre-depletion Enhances SCNT in Part through Derepression of Minor ZGA Genes

We then asked whether gene expression may be altered in SCNT embryos upon cohesin pre-depletion. Major zygotic genome activation (ZGA) occurs at the late 2-cell stage in mouse embryos, when thousands of genes start to express (Lee et al., 2014). RNA-seq analysis of cohesin-depleted SCNT embryos and controls (late 2-cell) showed that the global transcriptome is largely not affected (Figure 6A) and major ZGA is only moderately changed (Figure S7A). Surprisingly, minor ZGA genes (n = 72; FPKM [fragments per kilobase per million reads mapped] > 3 in fertilized early 2-cell; FPKM < 1 both in germinal vesicle [GV] oocyte and MII oocyte) are unexpectedly upregulated upon cohesin pre-depletion (Figure 6A). These genes are mainly transcribed at the late 1-cell and early 2-cell stage (Lee et al., 2014), as well as the 2-cell-like mESCs (Macfarlan et al., 2012), but their transcripts are still detectable at the late 2-cell stage. Minor ZGA is essential for embryonic development, as transient inhibition of minor ZGA leads to 2-cell arrest of mouse embryos (Abe et al., 2018). Several minor genes are known to play critical roles in embryonic development, including *Zscan4*, which functions in telomere lengthening and embryo development (Falco et al., 2007; Ko, 2016). Importantly, minor ZGA genes are poorly activated in SCNT embryos (Matoba et al., 2014). A careful examination showed that about 47.8% of minor ZGA genes are activated upon cohesin pre-depletion ("cohesin dependent"), including *Zscan4* and *Usp17l*,

and the rest are not affected by cohesin pre-depletion ("cohesin independent"), including *Dux*, *Defb13*, and *Msx1* (Figure 6B). Interestingly, cohesin-dependent minor ZGA genes appear to be more enriched for those that normally express from early 2-cell stage but fail to be properly activated in SCNT embryos (Figure 6B). By contrast, cohesin-independent minor ZGA genes are more likely to initiate the transcription from 1-cell stage (PN5) and their activation is less affected in SCNT embryos. Hence, these data raise an interesting possibility that cohesin pre-depletion may rescue the activation of minor ZGA, which further promotes SCNT development.

Intriguingly, we also observed strong derepression of minor ZGA gene in cohesin-depleted donor cells (Figure 6C; differentiated mESCs). This is also true for undifferentiated mESCs and mESC-derived neurons specifically for cohesin-dependent group (Figures 6C, 6D, and S7B). To ask whether the derepression is a direct or indirect consequence of cohesin depletion, we performed a time course RNA-seq analysis of mESCs upon cohesin depletion. Several minor ZGA genes, such as *Zscan4a/b* and *Usp17lb*, were upregulated as early as 3 h after the auxin treatment (Figure 6C; see example in Figure 6E), suggesting that they are likely direct targets of cohesin. Of note, transcripts of cohesin-dependent minor ZGA genes were not detected in 1-cell SCNT embryos, suggesting that those in 2-cell SCNT embryos are transcribed from embryos, rather than "carryover" from donor cells (Figure 6B).

Next, we asked whether the derepression of minor ZGA genes directly promotes SCNT. *Zscan4* plays critical roles in early development (Falco et al., 2007), is among the earliest responders upon cohesin depletion, and can also activate other minor ZGA genes (Ko, 2016). Furthermore, it has been shown that overexpression of ZSCAN4 can promote SCNT (Yang et al., 2019). To test whether *Zscan4* partially explains the improved SCNT, we injected *Zscan4* small interfering RNAs (siRNAs) in MII oocytes, followed by enucleation and donor nucleus transfer. The *Zscan4* knockdown efficiency was validated in the late 2-cell SCNT embryos (Figure S7C). Interestingly, other minor ZGA genes *Usp17la* and *Zfp352* were also downregulated as previously reported (Zhang et al., 2019). It is worth noting that the consecutive microinjection decreased the overall embryo viability for both control and *Zscan4* knockdown groups. Nevertheless, *Zscan4* knockdown reproducibly reduced blastocyst rates, although it did not reach statistical significance due to the small numbers of surviving blastocysts (Figures 6F and S7D). Taken together, these data indicate that the rescued minor ZGA upon cohesin pre-depletion may play a key role in the improved SCNT efficiency.

Figure 5. Pre-depletion of Cohesin from Donor Cells Improves SCNT Efficiency

(A) Schematic showing the experimental flow. To mimic the somatic cell chromatin state, mESCs were differentiated by withdrawing LIF for 3 days. The degradation of cohesin (SCC1) was induced by auxin treatment for 1 day in the experiment group.

(B) Left: heatmaps showing the normalized average interaction frequencies for all TADs (defined in mESC) as well as their nearby regions (±0.5 TAD length) in SCC1 WT (SCC1+) or depleted (SCC1−) donor cells or the derived SCNT 1-cell (PPN1) embryos. Right: the average insulation scores of SCC1 WT (SCC1+) or depleted (SCC1−) donor cells or the derived SCNT 1-cell (PPN1) embryos at TADs (defined in mESC) and nearby regions (±0.5 TAD length) are shown.

(C) Bar charts showing the developmental ratio (numbers of blastocysts divided by the numbers of 1-cell embryos) for SCNT embryos derived from control or cohesin-depleted nuclei. The total numbers of SCNT 1-cell embryos combined from four replicates are shown. Error bars denote the standard error of mean. p values calculated by t test (two-tailed) are also shown.

(D) Images of SCNT embryos derived from control or SCC1-depleted nuclei. Arrows indicate successful developed SCNT blastocysts (bar: 50 μm). Enlarged views of blastocysts (from dashed boxes) are also shown.

See also Figure S6 and Table S2.
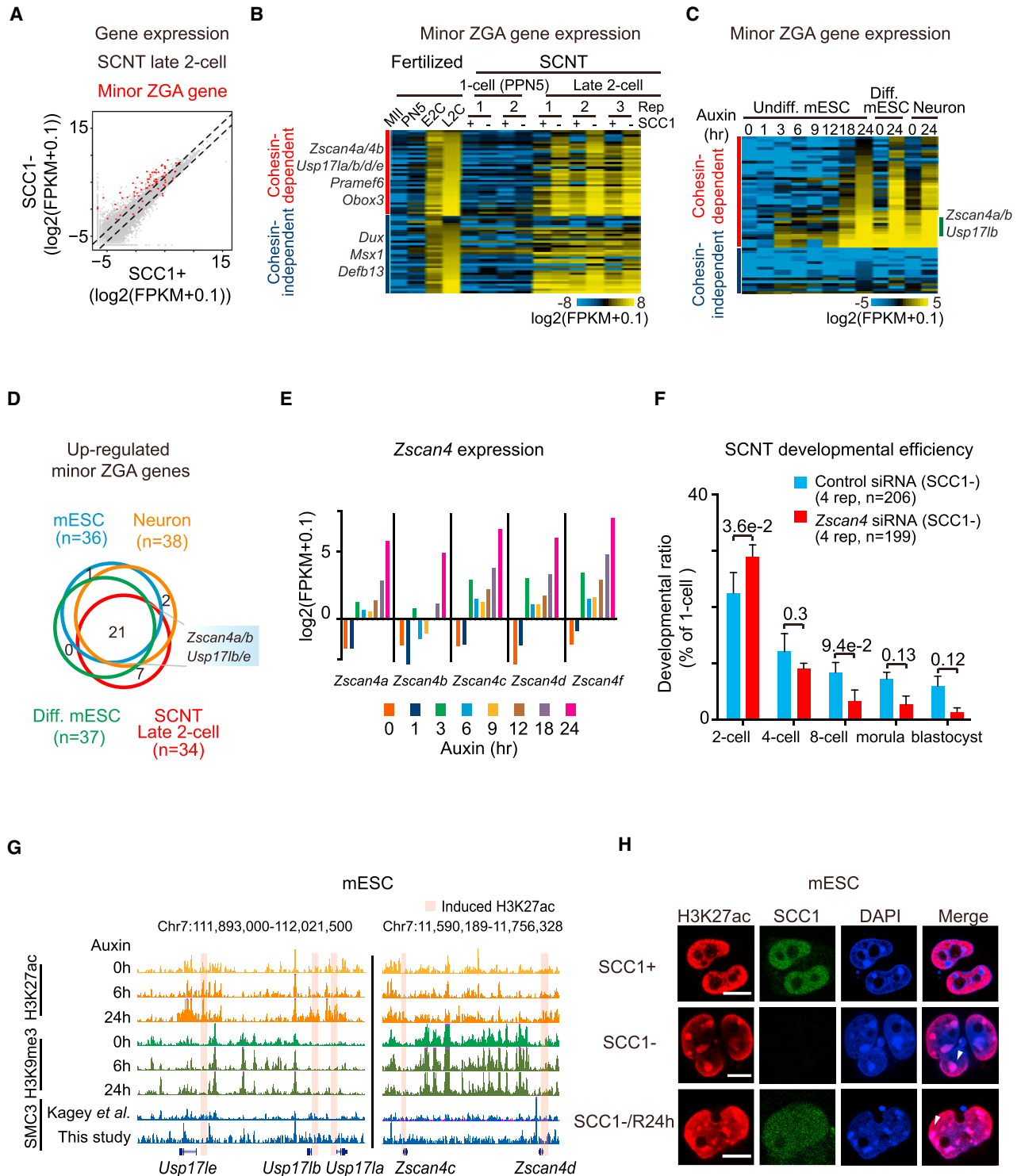
Figure 6. Cohesin Pre-depletion Enhances SCNT in Part through Derepression of Minor ZGA Genes

(A) Scatterplot comparing the transcriptomes of SCNT late 2-cell embryos between those derived from WT and cohesin-depleted cells. Red, minor ZGA genes. Dashed lines indicate the gene expression level fold changes of 0.5 and 2.

(B) Heatmap showing the minor ZGA gene expression in MII oocytes, fertilized PN5 1-cell embryos, fertilized early 2-cell (E2C), fertilized late 2-cell (L2C), SCNT 1-cell (PPN5), and late 2-cell embryos derived from WT or cohesin-depleted cells. Rep, replicate.

As the global TADs are already restored in SCNT 1-cell embryos (Figure 5B), these data raise an interesting possibility that the chromatin states of minor ZGA genes may have been changed upon cohesin depletion, and such changes then persist to late 2-cell embryos despite the restoration of cohesin, ultimately allowing the activation of minor ZGA genes. Of note, analysis of published data (Kagey et al., 2010) and data in this study failed to detect cohesin (SMC3) at minor ZGA gene promoters in mESCs, with most cohesin peaks appearing on average 80–200 kb away (Figures S7E and S7F), thus arguing against a role of cohesin directly at gene promoters. Given cohesin can translocate along chromatin and lacks specific DNA binding motifs (Nasmyth and Haering, 2009), it is possible that it may exert repression by facilitating the higher order assembly of repressive chromatin through non-specific DNA binding that cannot be directly measured by chromatin immunoprecipitation sequencing (ChIP-seq). In fact, many minor ZGA genes (such as *Zscan4* and *Usp17l*) exist as clusters and reside in "micro-heterochromatin" (Ko, 2016). Heterochromatin derepression is observed in 2-cell-like ESCs, a transient cell state when several 2-cell-specific genes, including *Zscan4*, are expressed (Akiyama et al., 2015). We did not observe obvious changes of H3K9me3, a heterochromatin histone mark, upon depletion of cohesin in the donor cells (Figures 6G and S7G), although we cannot exclude the possibility that such changes may occur only in a fraction of cells. However, ChIP-seq revealed increased H3K27ac near derepressed minor ZGA gene promoters (Figures 6G and S7G). Furthermore, we also observed ectopic H3K27ac in DAPI-dense heterochromatin in a small fraction of donor cells (14.9%), which persisted at least 24 h even after cohesin recovery (auxin wash-off; termed SCC1-/R24h; Figures 6H and S7H). Notably, as both fertilized and SCNT 1-cell and late 2-cell embryos (including wild type [WT]) lack DAPI-dense puncta (Figure S7I) as previously reported (Wongtawan et al., 2011), we could not investigate the states of heterochromatin upon cohesin pre-depletion in these embryos. Due to the extremely scarce materials, ChIP-seq of SCNT embryos is also not feasible at this moment. Thus, whether cohesin pre-depletion affects constitutive heterochromatin and chromatin near minor ZGA genes in SCNT embryos warrants future studies.

DISCUSSION

SCNT and Fertilization Share Features of 3D Genome Reprogramming

Transferring a somatic nucleus to oocyte can artificially convert a somatic cell to a totipotent state. However, the molecular basis for the chromatin reprogramming in this process remains poorly studied. Here, using a low-input Hi-C (sisHi-C) approach, we provided a spatiotemporal view of highly dynamic chromatin structure during SCNT (Figure 7A). Despite examples of epigenetic inheritance, such as imprints, the emerging picture appears to indicate that the majority of epigenetic parental memory is lost after fertilization in mammals (Eckersley-Maslin et al., 2018; Xu and Xie, 2018), presumably to efficiently kick-start the embryonic program. Previously, we and others have reported that TADs are strongly depleted in early embryos of fly, fish, mouse, and human (Figure 7A; Chen et al., 2019; Du et al., 2017; Hug et al., 2017; Kaaij et al., 2018; Ke et al., 2017; Nakamura et al., 2018), proving that this is a highly conserved feature during evolution. However, how this occurs and the role of the relaxed chromatin structure in early embryos remain a mystery. Here, we showed that similar observation was also made in SCNT embryos for TADs (2-cell) and chromatin compartments (1-cell). This agrees with a recent study (Chen et al., 2020) and is consistent with the notion that somatic nuclei show increased DNase I sensitivity after being transferred to enucleated oocytes (Kim et al., 2002), suggesting that ooplasm has a unique ability to convert chromatin to a relaxed state, regardless of the chromatin origin.

SCNT and Fertilization Also Show Differential 3D Genome Reprogramming

The 3D chromatin dynamics of SCNT also show notable differences from that in fertilized embryos. In particular, the initial de-compaction of chromatin organization appears to be less efficient or delayed in SCNT embryos. Mechanistically, what contributes to such differences? One potential factor is the differential chromatin architectural proteins between gametes and somatic cells. For example, mouse oocytes express meiosis-specific klesin subunit of cohesin, such as RAD21L and REC8 (McNicoll et al., 2013). It is possible that ooplasm has dedicated machinery that can efficiently relax meiotic cohesin-mediated chromatin organization after fertilization. In addition, protamines from sperm are swiftly replaced by histones after fertilization (Sassone-Corsi, 2002). It remains to be tested whether the protamine-histone exchange may also promote 3D genome reprogramming. Of note, we could not rule out the possibility that, in SCNT, a minor fraction of embryos may undergo efficient TAD relaxation but are masked in the bulk data, and the relaxed TADs in 2-cell SCNT embryos may reflect a development selection of these embryos from 1-cell embryos.

(C) Heatmap showing the minor ZGA gene expression dynamics in mESCs, differentiated cells, and mESC-derived neurons after cohesin depletion. The minor ZGA genes that are already highly expressed in mESC prior to cohesin depletion were excluded.

(D) Venn diagram shows the overlap of derepressed minor ZGA genes among SCNT late 2-cell embryos, mESCs, differentiated mESCs, and mESC-derived neurons upon the removal of cohesin. Example genes shared by all four groups are listed.
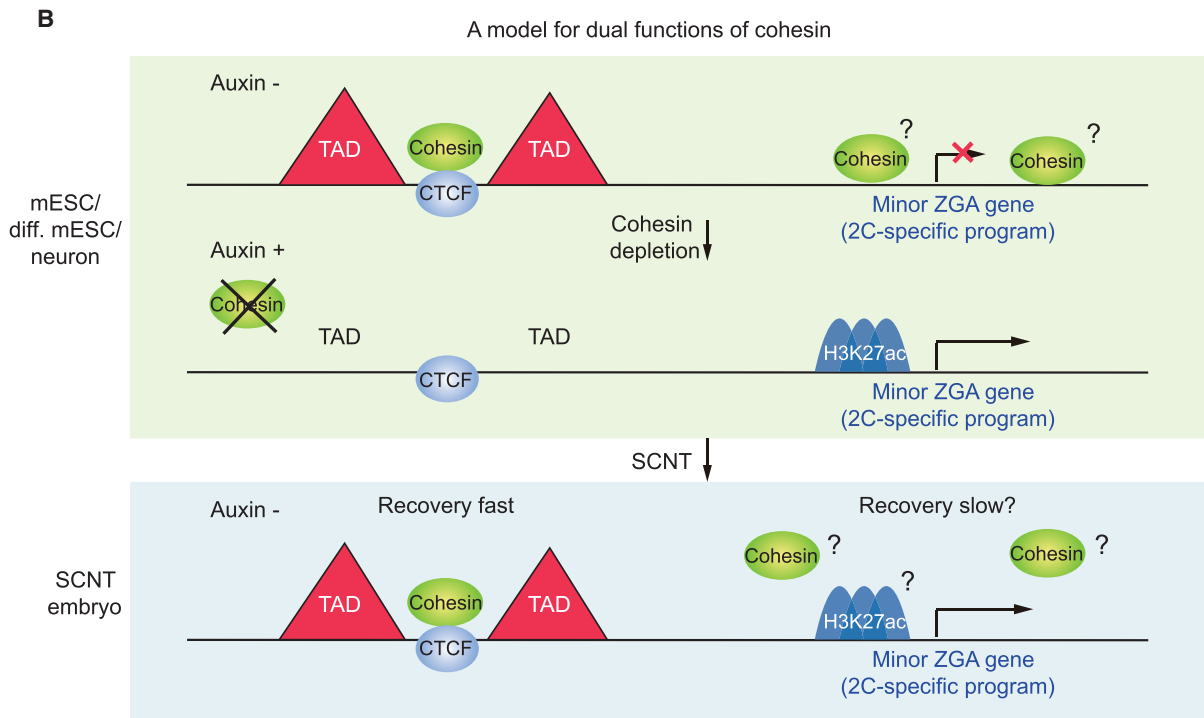
(E) Bar charts showing the dynamics of *Zscan4* family expression in mESC after cohesin depletion.

(F) Bar charts showing the developmental ratio (blastocysts/1-cell embryos) for SCNT embryos derived from oocytes injected with either *Zscan4* siRNA or control siRNA (SCC1-depleted cells were used as the donor cells). The total numbers of SCNT 1-cell embryos combined from four replicates are shown. Error bars denote the standard error of mean. p values calculated by t test (two-tailed) are also shown.

(G) UCSC tracks showing the ChIP-seq enrichment of H3K9me3 and H3K27ac upon SCC1 depletion for the *Usp17l* and *Zscan4* clusters. Increased H3K27ac near promoters is shaded. The binding of cohesin (SMC3 previously published [Kagey et al., 2010] or generated in this study) in mESCs is also shown.

(H) Immunofluorescence staining of H3K27ac in mESCs before auxin treatment, 24 h after auxin treatment, and 24 h after auxin wash away (bar: 10 μm).

See also Figure S7.

A

Fertilization

Sperm + MII oocyte

1-cell   2-cell   8-cell   Blastocyst rate
+++

TAD

Minor ZGA   Major ZGA

mESC/diff. mESC/neuron

SCNT

Cohesin

Minor ZGA gene (2C-specific program) ✗

SCNT

Donor: diff. mESC

1-cell   2-cell   8-cell   Blastocyst rate
+

TAD

Minor ZGA   Major ZGA

+

Cohesin

Minor ZGA gene (2C-specific program) ✓

Enucleated oocyte

SCNT

Blastocyst rate
++

TAD

Minor ZGA   Major ZGA

B   A model for dual functions of cohesin

mESC/diff. mESC/neuron

Auxin -

TAD   Cohesin   TAD
       CTCF

Cohesin ?   ✗   Cohesin ?

Minor ZGA gene (2C-specific program)

Auxin +

Cohesin ✗

TAD   TAD
    CTCF

Cohesin depletion ↓

H3K27ac

Minor ZGA gene (2C-specific program)

SCNT ↓

SCNT embryo

Auxin -   Recovery fast   Recovery slow?

TAD   Cohesin   TAD
       CTCF

Cohesin ?   ?   Cohesin ?

H3K27ac

Minor ZGA gene (2C-specific program)

(legend on next page)

Pre-depletion of Cohesin from Donor Cells Improves SCNT Efficiency

Insufficient removal of parental epigenetic marks is known to impede SCNT development (Matoba and Zhang, 2018). Despite the efforts to correct such aberrant epigenetic memory, only a small fraction of SCNT mouse embryos can proceed to term (Matoba and Zhang, 2018). Thus, identifying the remaining epigenetic barrier is a key question in the field. Interestingly, we found that pre-depletion of cohesin in donor cells facilitates SCNT development. Unexpectedly, this is linked to the derepression of minor ZGA genes, the activation of which is typically defective in SCNT. How cohesin represses minor ZGA genes remains unclear at this moment. In mESCs, cohesin does not typically bind promoters of minor ZGA genes. Given the derepressed genes are often gene families residing in clusters, it is possible that cohesin may be involved in certain higher order chromatin structure assembly through non-specific DNA binding that cannot be directly measured by ChIP-seq. For instance, condensin, a protein complex related to cohesin, mediates condensation of mitotic chromatin through the assembly of random loops without binding to defined chromatin loci (Gibcus et al., 2018; Naumova et al., 2013). Notably, a recent study revealed that the knockdown of *Smchd1* (a non-canonical cohesin) in mouse zygote also results in overexpression of *Zscan4* in 2-cell embryos (Ruebel et al., 2019). SMCHD1 is known to repress inactive X chromosome and a limited set of autosomal gene clusters that often reside in micro-heterochromatin (Jansz et al., 2017). In human somatic cells, mutations of *Smchd1* cause relaxation of the D4Z4 macrosatellite array and the derepression of the embedded DUX4 gene, leading to facioscapulohumeral dystrophy (FSHD), a facial and upper-extremity muscle disease (Jansz et al., 2017). As SCC1 depletion does not derepress *Dux* (Figure 6B) and SMCHD1 expels cohesin on the inactive X chromosome (Gdula et al., 2019; Wang et al., 2018), SMCHD1 and canonical cohesin may act in partially overlapping yet non-identical pathways in repressing minor ZGA genes.

In sum, these data suggest two possibly distinct functions of cohesin (Figure 7B). Cohesin works with CTCF to establish TADs. Meanwhile, it also represses minor ZGA genes. Upon cohesin removal in donor cells, TADs are lost and minor ZGA genes are activated. After nuclear transfer, the lack of auxin quickly restores global TADs in SCNT 1-cell embryos. However, chromatin defects at minor ZGA genes likely recover slowly, if not at all, allowing the activation of minor ZGA genes and improved SCNT development. Notably, the restoration of global TADs in 1-cell SCNT embryos does not exclude the possibility that TADs are reprogrammed at specific loci. Whether the relaxation and re-establishment of TADs reset chromatin architecture and related regulatory network (such as promoter-enhancer pairs) during parental-to-zygotic transition requires fine-scale analyses and are exciting topics for future investigations.

STAR★METHODS

Detailed methods are provided in the online version of this paper and include the following:

- KEY RESOURCES TABLE
- RESOURCE AVAILABILITY
  - Lead Contact
  - Materials Availability
  - Data and Code Availability
- EXPERIMENTAL MODEL AND SUBJECT DETAILS
  - Animals
  - Cell lines
  - Primary cell culture
- METHOD DETAILS
  - Donor cell preparation
  - Nuclear transfer
  - Knockdown of Zscan4 in cloned embryos
  - Neuron differentiation
  - DAPI staining
  - Immunostaining
  - sisHi-C library generation and sequencing
  - RNA-seq library preparation and sequencing
  - ChIP-seq library generation and sequencing
  - CUT&RUN library generation and sequencing
  - Data analysis
- QUANTIFICATION AND STATISTICAL ANALYSIS

Figure 7. The Schematic Model for the 3D Chromatin Reprogramming during Fertilization and SCNT

(A) Schematic model comparing the reprogramming of chromatin organization in fertilized and SCNT embryo development. For fertilized embryos, TADs are highly relaxed after fertilization and become increasingly consolidated during early development. For SCNT, TADs undergo partial dissolution after nuclear transfer (not shown). However, TADs are stronger in 1-cell SCNT embryos compared to fertilized embryos before they become diminished at the late 2-cell stage. TADs then become consolidated at the 8-cell stage again. Minor ZGA genes activation is defective in SCNT. Cohesin can repress minor ZGA genes in mESCs, differentiated mESCs, and mESC-derived neurons. Pre-depletion of cohesin in donor cells promotes minor ZGA and SCNT development.

(B) A model for dual functions of cohesin. Cohesin functions together with CTCF to establish TADs. Meanwhile, it also represses minor ZGA genes. Cohesin removal results in loss of TADs, derepression of minor ZGA genes, and perhaps relaxation of heterochromatin (increased histone acetylation) in donor cells. After nuclear transfer, the lack of auxin quickly restores TADs in SCNT 1-cell embryos. However, chromatin defects at minor ZGA genes likely recover slowly, if not at all, allowing activation of minor ZGA genes and improved SCNT development.

AUTHOR CONTRIBUTIONS

D.W., X.L., L.W., and W.Xiong performed the mouse somatic nuclear transfer experiments. K.Z. conducted the sisHi-C experiments. H.Z., K.Z., and Y.W. performed bioinformatics analysis. K.Z., D.W., Q.S., X.L., and Q.W. performed cell culture and conducted RNA-seq. Y.W. and L.L. conducted the ChIP experiments. Q.W. performed NGS sequencing. J.D.P.R. generated the SCC1-AID mESC cell line. K.X., Z.L., G.Y., W. Xia, B.H., Z.D., and Y.Y. helped with various experiments or analyses. K.A.N., R.J.K., Y.M., and W. Xie supervised the project or related experiments. K.Z., H.Z., D.W., Y.W., Y.M., and W. Xie prepared the manuscript with help from all authors.

DECLARATION OF INTERESTS

The authors declare no competing interests.

REFERENCES

Abe, K.I., Funaya, S., Tsukioka, D., Kawamura, M., Suzuki, Y., Suzuki, M.G., Schultz, R.M., and Aoki, F. (2018). Minor zygotic gene activation is essential for mouse preimplantation development. Proc. Natl. Acad. Sci. USA *115*, E6780–E6788.

Ahmed, K., Dehghani, H., Rugg-Gunn, P., Fussner, E., Rossant, J., and Bazett-Jones, D.P. (2010). Global chromatin architecture reflects pluripotency and lineage commitment in the early mouse embryo. PLoS ONE *5*, e10531.

Akdemir, K.C., and Chin, L. (2015). HiCPlotter integrates genomic data with interaction matrices. Genome Biol. *16*, 198.

Akiyama, T., Xin, L., Oda, M., Sharov, A.A., Amano, M., Piao, Y., Cadet, J.S., Dudekula, D.B., Qian, Y., Wang, W., et al. (2015). Transient bursts of Zscan4 expression are accompanied by the rapid derepression of heterochromatin in mouse embryonic stem cells. DNA Res. *22*, 307–318.

Allis, C.D., and Jenuwein, T. (2016). The molecular hallmarks of epigenetic control. Nat. Rev. Genet. *17*, 487–500.

Barutcu, A.R., Maass, P.G., Lewandowski, J.P., Weiner, C.L., and Rinn, J.L. (2018). A TAD boundary is preserved upon deletion of the CTCF-rich Firre locus. Nat. Commun. *9*, 1444.

Battulin, N., Fishman, V.S., Mazur, A.M., Pomaznoy, M., Khabarova, A.A., Afonnikov, D.A., Prokhortchouk, E.B., and Serov, O.L. (2015). Comparison of the three-dimensional organization of sperm and fibroblast genomes using the Hi-C approach. Genome Biol. *16*, 77.

Bickmore, W.A. (2013). The spatial organization of the human genome. Annu. Rev. Genomics Hum. Genet. *14*, 67–84.

Bolstad, B.M., Irizarry, R.A., Åstrand, M., and Speed, T.P. (2003). A comparison of normalization methods for high density oligonucleotide array data based on variance and bias. Bioinformatics *19* (2), 185–193.

Brind'Amour, J., Liu, S., Hudson, M., Chen, C., Karimi, M.M., and Lorincz, M.C. (2015). An ultra-low-input native ChIP-seq protocol for genome-wide profiling of rare cell populations. Nat. Commun. *6*, 6033.

Campbell, K.H., Loi, P., Otaegui, P.J., and Wilmut, I. (1996). Cell cycle co-ordination in embryo cloning by nuclear transfer. Rev. Reprod. *1*, 40–46.

Chen, X., Ke, Y., Wu, K., Zhao, H., Sun, Y., Gao, L., Liu, Z., Zhang, J., Tao, W., Hou, Z., et al. (2019). Key role for CTCF in establishing chromatin structure in human embryos. Nature *576*, 306–310.

Chen, M., Zhu, Q., Li, C., Kou, X., Zhao, Y., Li, Y., Xu, R., Yang, L., Yang, L., Gu, L., et al. (2020). Chromatin architecture reorganization in murine somatic cell nuclear transfer embryos. Nat. Commun. *11*, 1813.

Chung, B.M., Kang, H.C., Han, S.Y., Heo, H.S., Lee, J.J., Jeon, J., Lim, J.Y., Shin, I., Hong, S.H., Cho, Y.S., and Kim, C.G. (2006). Jak2 and Tyk2 are necessary for lineage-specific differentiation, but not for the maintenance of self-renewal of mouse embryonic stem cells. Biochem. Biophys. Res. Commun. *351*, 682–688.

Collombet, S., Ranisavljevic, N., Nagano, T., Varnai, C., Shisode, T., Leung, W., Piolot, T., Galupa, R., Borensztein, M., Servant, N., et al. (2020). Parental-to-embryo switch of chromosome organization in early embryogenesis. Nature *580*, 142–146.

Crane, E., Bian, Q., McCord, R.P., Lajoie, B.R., Wheeler, B.S., Ralston, E.J., Uzawa, S., Dekker, J., and Meyer, B.J. (2015). Condensin-driven remodelling of X chromosome topology during dosage compensation. Nature *523*, 240–244.

Davidson, I.F., Bauer, B., Goetz, D., Tang, W., Wutz, G., and Peters, J.M. (2019). DNA loop extrusion by human cohesin. Science *366*, 1338–1345.

de Hoon, M.J.L., Imoto, S., Nolan, J., and Miyano, S. (2004). Open source clustering software. Bioinformatics *20*, 1453–1454.

Dixon, J.R., Jung, I., Selvaraj, S., Shen, Y., Antosiewicz-Bourget, J.E., Lee, A.Y., Ye, Z., Kim, A., Rajagopal, N., Xie, W., et al. (2015). Chromatin architecture reorganization during stem cell differentiation. Nature *518*, 331–336.

Djekidel, M.N., Inoue, A., Matoba, S., Suzuki, T., Zhang, C., Lu, F., Jiang, L., and Zhang, Y. (2018). Reprogramming of chromatin accessibility in somatic cell nuclear transfer is DNA replication independent. Cell Rep. *23*, 1939–1947.

Du, Z., Zheng, H., Huang, B., Ma, R., Wu, J., Zhang, X., He, J., Xiang, Y., Wang, Q., Li, Y., et al. (2017). Allelic reprogramming of 3D chromatin architecture during early mammalian development. Nature *547*, 232–235.

Eckersley-Maslin, M.A., Alda-Catalinas, C., and Reik, W. (2018). Dynamics of the epigenetic landscape during the maternal-to-zygotic transition. Nat. Rev. Mol. Cell Biol. *19*, 436–450.

Falco, G., Lee, S.-L., Stanghellini, I., Bassey, U.C., Hamatani, T., and Ko, M.S.H. (2007). Zscan4: a novel gene expressed exclusively in late 2-cell embryos and embryonic stem cells. Dev. Biol. *307*, 539–550.

Flyamer, I.M., Gassler, J., Imakaev, M., Brandão, H.B., Ulianov, S.V., Abdennur, N., Razin, S.V., Mirny, L.A., and Tachibana-Konwalski, K. (2017). Single-nucleus Hi-C reveals unique chromatin reorganization at oocyte-to-zygote transition. Nature *544*, 110–114.

Fudenberg, G., Imakaev, M., Lu, C., Goloborodko, A., Abdennur, N., and Mirny, L.A. (2016). Formation of chromosomal domains by loop extrusion. Cell Rep. *15*, 2038–2049.

Gao, S., McGarry, M., Latham, K.E., and Wilmut, I. (2003). Cloning of mice by nuclear transfer. Cloning Stem Cells *5*, 287–294.

Gassler, J., Brandão, H.B., Imakaev, M., Flyamer, I.M., Ladstätter, S., Bickmore, W.A., Peters, J.M., Mirny, L.A., and Tachibana, K. (2017). A mechanism of cohesin-dependent loop extrusion organizes zygotic genome architecture. EMBO J. *36*, 3600–3618.

Gdula, M.R., Nesterova, T.B., Pintacuda, G., Godwin, J., Zhan, Y., Ozadam, H., McClellan, M., Moralli, D., Krueger, F., Green, C.M., et al. (2019). The non-canonical SMC protein SmcHD1 antagonises TAD formation and compartmentalisation on the inactive X chromosome. Nat. Commun. *10*, 30.

Gibcus, J.H., and Dekker, J. (2013). The hierarchy of the 3D genome. Mol. Cell *49*, 773–782.

Gibcus, J.H., Samejima, K., Goloborodko, A., Samejima, I., Naumova, N., Nuebler, J., Kanemaki, M.T., Xie, L., Paulson, J.R., Earnshaw, W.C., et al. (2018). A pathway for mitotic chromosome formation. Science *359*, eaao6135.

Gorkin, D.U., Leung, D., and Ren, B. (2014). The 3D genome in transcriptional regulation and pluripotency. Cell Stem Cell *14*, 762–775.

Grunstein, M. (1997). Histone acetylation in chromatin structure and transcription. Nature *389*, 349–352.

Gurdon, J.B. (2006). From nuclear transfer to nuclear reprogramming: the reversal of cell differentiation. Annu. Rev. Cell Dev. Biol. *22*, 1–22.

Haarhuis, J.H.I., van der Weide, R.H., Blomen, V.A., Yáñez-Cuna, J.O., Amendola, M., van Ruiten, M.S., Krijger, P.H.L., Teunissen, H., Medema, R.H., van Steensel, B., et al. (2017). The cohesin release factor WAPL restricts chromatin loop extension. Cell *169*, 693–707.e14.

Hendrickson, P.G., Doráis, J.A., Grow, E.J., Whiddon, J.L., Lim, J.-W., Wike, C.L., Weaver, B.D., Pflueger, C., Emery, B.R., Wilcox, A.L., et al. (2017). Conserved roles of mouse DUX and human DUX4 in activating cleavage-stage genes and MERVL/HERVL retrotransposons. Nat. Genet. *49*, 925–934.

Hug, C.B., Grimaldi, A.G., Kruse, K., and Vaquerizas, J.M. (2017). Chromatin architecture emerges during zygotic genome activation independent of transcription. Cell *169*, 216–228.e19.

Imakaev, M., Fudenberg, G., McCord, R.P., Naumova, N., Goloborodko, A., Lajoie, B.R., Dekker, J., and Mirny, L.A. (2012). Iterative correction of Hi-C data reveals hallmarks of chromosome organization. Nat. Methods *9*, 999–1003.

Ishiguro, K.I., Monti, M., Akiyama, T., Kimura, H., Chikazawa-Nohtomi, N., Sakota, M., Sato, S., Redi, C.A., Ko, S.B.H., and Ko, M.S.H. (2017). Zscan4 is expressed specifically during late meiotic prophase in both spermatogenesis and oogenesis. In Vitro Cell. Dev. Biol. Anim. *53*, 167–178.

Jansz, N., Chen, K., Murphy, J.M., and Blewitt, M.E. (2017). The epigenetic regulator SMCHD1 in development and disease. Trends Genet. *33*, 233–243.

Jung, Y.H., Sauria, M.E.G., Lyu, X., Cheema, M.S., Ausio, J., Taylor, J., and Corces, V.G. (2017). Chromatin states in mouse sperm correlate with embryonic and adult regulatory landscapes. Cell Rep. *18*, 1366–1382.

Kaaij, L.J.T., van der Weide, R.H., Ketting, R.F., and de Wit, E. (2018). Systemic loss and gain of chromatin architecture throughout zebrafish development. Cell Rep. *24*, 1–10.e4.

Kagey, M.H., Newman, J.J., Bilodeau, S., Zhan, Y., Orlando, D.A., van Berkum, N.L., Ebmeier, C.C., Goossens, J., Rahl, P.B., Levine, S.S., et al. (2010). Mediator and cohesin connect gene expression and chromatin architecture. Nature *467*, 430–435.

Ke, Y., Xu, Y., Chen, X., Feng, S., Liu, Z., Sun, Y., Yao, X., Li, F., Zhu, W., Gao, L., et al. (2017). 3D chromatin structures of mature gametes and structural reprogramming during mammalian embryogenesis. Cell *170*, 367–381.e20.

Kim, J.-M., Ogura, A., Nagata, M., and Aoki, F. (2002). Analysis of the mechanism for chromatin remodeling in embryos reconstructed by somatic nuclear transfer. Biol. Reprod. *67*, 760–766.

Kim, D., Pertea, G., Trapnell, C., Pimentel, H., Kelley, R., and Salzberg, S.L. (2013). TopHat2: accurate alignment of transcriptomes in the presence of insertions, deletions and gene fusions. Genome Biol. *14*, R36.

Kim, Y., Shi, Z., Zhang, H., Finkelstein, I.J., and Yu, H. (2019). Human cohesin compacts DNA by loop extrusion. Science *366*, 1345–1349.

Kishigami, S., Mizutani, E., Ohta, H., Hikichi, T., Thuan, N.V., Wakayama, S., Bui, H.-T., and Wakayama, T. (2006). Significant improvement of mouse cloning technique by treatment with trichostatin A after somatic nuclear transfer. Biochem. Biophys. Res. Commun. *340*, 183–189.

Ko, M.S. (2016). Zygotic genome activation revisited: looking through the expression and function of Zscan4. Curr. Top. Dev. Biol. *120*, 103–124.

Kretsovali, A., Hadjimichael, C., and Charmpilas, N. (2012). Histone deacetylase inhibitors in cell pluripotency, differentiation, and reprogramming. Stem Cells Int. *2012*, 184154.

Langmead, B., and Salzberg, S.L. (2012). Fast gapped-read alignment with Bowtie 2. Nat. Methods *9*, 357–359.

Lee, M.T., Bonneau, A.R., and Giraldez, A.J. (2014). Zygotic genome activation during the maternal-to-zygotic transition. Annu. Rev. Cell Dev. Biol. *30*, 581–613.

Li, H., Handsaker, B., Wysoker, A., Fennell, T., Ruan, J., Homer, N., Marth, G., Abecasis, G., and Durbin, R.; 1000 Genome Project Data Processing

Subgroup (2009). The Sequence Alignment/Map format and SAMtools. Bioinformatics *25*, 2078–2079.

Lieberman-Aiden, E., van Berkum, N.L., Williams, L., Imakaev, M., Ragoczy, T., Telling, A., Amit, I., Lajoie, B.R., Sabo, P.J., Dorschner, M.O., et al. (2009). Comprehensive mapping of long-range interactions reveals folding principles of the human genome. Science *326*, 289–293.

Liu, W., Liu, X., Wang, C., Gao, Y., Gao, R., Kou, X., Zhao, Y., Li, J., Wu, Y., Xiu, W., et al. (2016). Identification of key factors conquering developmental arrest of somatic cell cloned embryos by combining embryo biopsy and single-cell sequencing. Cell Discov. *2*, 16010.

Liu, Y., Wu, F., Zhang, L., Wu, X., Li, D., Xin, J., Xie, J., Kong, F., Wang, W., Wu, Q., et al. (2018). Transcriptional defects and reprogramming barriers in somatic cell nuclear reprogramming as revealed by single-embryo RNA sequencing. BMC Genomics *19*, 734.

Macfarlan, T.S., Gifford, W.D., Driscoll, S., Lettieri, K., Rowe, H.M., Bonanomi, D., Firth, A., Singer, O., Trono, D., and Pfaff, S.L. (2012). Embryonic stem cell potency fluctuates with endogenous retrovirus activity. Nature *487*, 57–63.

MacGregor, I.A., Adams, I.R., and Gilbert, N. (2019). Large-scale chromatin organisation in interphase, mitosis and meiosis. Biochem. J. *476*, 2141–2156.

Matoba, S., and Zhang, Y. (2018). Somatic cell nuclear transfer reprogramming: mechanisms and applications. Cell Stem Cell *23*, 471–485.

Matoba, S., Liu, Y., Lu, F., Iwabuchi, K.A., Shen, L., Inoue, A., and Zhang, Y. (2014). Embryonic development following somatic cell nuclear transfer impeded by persisting histone methylation. Cell *159*, 884–895.

McNicoll, F., Stevense, M., and Jessberger, R. (2013). Cohesin in gametogenesis. Curr. Top. Dev. Biol. *102*, 1–34.

Nagano, T., Lubling, Y., Várnai, C., Dudley, C., Leung, W., Baran, Y., Mendelson Cohen, N., Wingett, S., Fraser, P., and Tanay, A. (2017). Cell-cycle dynamics of chromosomal organization at single-cell resolution. Nature *547*, 61–67.

Nakamura, R., Motai, Y., Kumagai, M., Nishiyama, H., Durand, N.C., Kondo, K., Kondo, T., Tsukahara, T., Shimada, A., and Aiden, E.L. (2018). CTCF looping is established during gastrulation in medaka embryos. bioRxiv. https://doi.org/10.1101/454082.

Nasmyth, K., and Haering, C.H. (2009). Cohesin: its roles and mechanisms. Annu. Rev. Genet. *43*, 525–558.

Naumova, N., Imakaev, M., Fudenberg, G., Zhan, Y., Lajoie, B.R., Mirny, L.A., and Dekker, J. (2013). Organization of the mitotic chromosome. Science *342*, 948–953.

Paradis, E., Claude, J., and Strimmer, K. (2004). APE: analyses of phylogenetics and evolution in R language. Bioinformatics *20*, 289–290.

Picelli, S., Faridani, O.R., Björklund, A.K., Winberg, G., Sagasser, S., and Sandberg, R. (2014). Full-length RNA-seq from single cells using Smart-seq2. Nat. Protoc. *9*, 171–181.

Pombo, A., and Dillon, N. (2015). Three-dimensional genome architecture: players and mechanisms. Nat. Rev. Mol. Cell Biol. *16*, 245–257.

Quinlan, A.R., and Hall, I.M. (2010). BEDTools: a flexible suite of utilities for comparing genomic features. Bioinformatics *26*, 841–842.

Quinodoz, S.A., Ollikainen, N., Tabak, B., Palla, A., Schmidt, J.M., Detmar, E., Lai, M.M., Shishkin, A.A., Bhat, P., Takei, Y., et al. (2018). Higher-order inter-chromosomal hubs shape 3D genome organization in the nucleus. Cell *174*, 744–757.e24.

Ramírez, F., Ryan, D.P., Grüning, B., Bhardwaj, V., Kilpert, F., Richter, A.S., Heyne, S., Dündar, F., and Manke, T. (2016). deepTools2: a next generation web server for deep-sequencing data analysis. Nucleic Acids Res. *44* (W1), W160–W165.

Rao, S.S.P., Huang, S.C., Glenn St Hilaire, B., Engreitz, J.M., Perez, E.M., Kieffer-Kwon, K.R., Sanborn, A.L., Johnstone, S.E., Bascom, G.D., Bochkov, I.D., et al. (2017). Cohesin loss eliminates all loop domains. Cell *171*, 305–320.e24.

Rhodes, J.D.P., Feldmann, A., Hernández-Rodríguez, B., Díaz, N., Brown, J.M., Fursova, N.A., Blackledge, N.P., Prathapan, P., Dobrinic, P., Huseyin,

M.K., et al. (2020). Cohesin disrupts polycomb-dependent chromosome interactions in embryonic stem cells. Cell Rep. *30*, 820–835.e10.

Rowley, M.J., and Corces, V.G. (2016). The three-dimensional genome: principles and roles of long-distance interactions. Curr. Opin. Cell Biol. *40*, 8–14.

Ruebel, M.L., Vincent, K.A., Schall, P.Z., Wang, K., and Latham, K.E. (2019). SMCHD1 terminates the first embryonic genome activation event in mouse two-cell embryos and contributes to a transcriptionally repressive state. Am. J. Physiol. Cell Physiol. *317*, C655–C664.

Rybouchkin, A., Kato, Y., and Tsunoda, Y. (2006). Role of histone acetylation in reprogramming of somatic nuclei following nuclear transfer. Biol. Reprod. *74*, 1083–1089.

Saldanha, A.J. (2004). Java Treeview–extensible visualization of microarray data. Bioinformatics *20*, 3246–3248.

Sassone-Corsi, P. (2002). Unique chromatin remodeling and transcriptional regulation in spermatogenesis. Science *296*, 2176–2178.

Schwarzer, W., Abdennur, N., Goloborodko, A., Pekowska, A., Fudenberg, G., Loe-Mie, Y., Fonseca, N.A., Huber, W., Haering, C.H., Mirny, L., and Spitz, F. (2017). Two independent modes of chromatin organization revealed by cohesin removal. Nature *551*, 51–56.

Servant, N., Varoquaux, N., Lajoie, B.R., Viara, E., Chen, C.J., Vert, J.P., Heard, E., Dekker, J., and Barillot, E. (2015). HiC-Pro: an optimized and flexible pipeline for Hi-C data processing. Genome Biol. *16*, 259.

Shen, Y., Yue, F., McCleary, D.F., Ye, Z., Edsall, L., Kuan, S., Wagner, U., Dixon, J., Lee, L., Lobanenkov, V.V., and Ren, B. (2012). A map of the cis-regulatory sequences in the mouse genome. Nature *488*, 116–120.

Skene, P.J., and Henikoff, S. (2017). An efficient targeted nuclease strategy for high-resolution mapping of DNA binding sites. eLife *6*, e21856.

Trapnell, C., Roberts, A., Goff, L., Pertea, G., Kim, D., Kelley, D.R., Pimentel, H., Salzberg, S.L., Rinn, J.L., and Pachter, L. (2012). Differential gene and transcript expression analysis of RNA-seq experiments with TopHat and Cufflinks. Nat. Protoc. *7*, 562–578.

Ursu, O., Boley, N., Taranova, M., Wang, Y.X.R., Yardimci, G.G., Stafford Noble, W., and Kundaje, A. (2018). GenomeDISCO: a concordance score for chromosome conformation capture experiments using random walks on contact map graphs. Bioinformatics *34*, 2701–2707.

Wakayama, T., Perry, A.C., Zuccotti, M., Johnson, K.R., and Yanagimachi, R. (1998). Full-term development of mice from enucleated oocytes injected with cumulus cell nuclei. Nature *394*, 369–374.

Wang, C.Y., Jégu, T., Chu, H.P., Oh, H.J., and Lee, J.T. (2018). SMCHD1 merges chromosome compartments and assists formation of super-structures on the inactive X. Cell *174*, 406–421.e25.

Wongtawan, T., Taylor, J.E., Lawson, K.A., Wilmut, I., and Pennings, S. (2011). Histone H4K20me3 and HP1α are late heterochromatin markers in development, but present in undifferentiated embryonic stem cells. J. Cell Sci. *124*, 1878–1890.

Wu, M.Y., and Hill, C.S. (2009). Tgf-β superfamily signaling in embryonic development and homeostasis. Dev. Cell *16*, 329–343.

Xia, W., Xu, J., Yu, G., Yao, G., Xu, K., Ma, X., Zhang, N., Liu, B., Li, T., Lin, Z., et al. (2019). Resetting histone modifications during human parental-to-zygotic transition. Science *365*, 353–360.

Xu, Q., and Xie, W. (2018). Epigenome in early mammalian development: inheritance, reprogramming and establishment. Trends Cell Biol. *28*, 237–253.

Yang, L., Liu, X., Song, L., Su, G., Di, A., Bai, C., Wei, Z., and Li, G. (2019). Inhibiting repressive epigenetic modification promotes telomere rejuvenation in somatic cell reprogramming. FASEB J. *33*, 13982–13997.

Yardımcı, G.G., Ozadam, H., Sauria, M.E.G., Ursu, O., Yan, K.K., Yang, T., Chakraborty, A., Kaul, A., Lajoie, B.R., Song, F., et al. (2019). Measuring the reproducibility and quality of Hi-C data. Genome Biol. *20*, 57.

Zalzman, M., Falco, G., Sharova, L.V., Nishiyama, A., Thomas, M., Lee, S.L., Stagg, C.A., Hoang, H.G., Yang, H.T., Indig, F.E., et al. (2010). Zscan4 regulates telomere elongation and genomic stability in ES cells. Nature *464*, 858–863.

Zhang, Y., Liu, T., Meyer, C.A., Eeckhoute, J., Johnson, D.S., Bernstein, B.E., Nusbaum, C., Myers, R.M., Brown, M., Li, W., and Liu, X.S. (2008). Model-based analysis of ChIP-seq (MACS). Genome Biol. *9*, R137.

Zhang, W., Xia, W., Wang, Q., Towers, A.J., Chen, J., Gao, R., Zhang, Y., Yen, C.A., Lee, A.Y., Li, Y., et al. (2016). Isoform switch of TET1 regulates DNA demethylation and mouse development. Mol. Cell *64*, 1062–1073.

Zhang, W., Chen, F., Chen, R., Xie, D., Yang, J., Zhao, X., Guo, R., Zhang, Y., Shen, Y., Göke, J., et al. (2019). Zscan4c activates endogenous retrovirus MERVL and cleavage embryo genes. Nucleic Acids Res. *47*, 8485–8501.

Zheng, H., and Xie, W. (2019). The role of 3D genome organization in development and cell differentiation. Nat. Rev. Mol. Cell Biol. *20*, 535–550.

Zheng, H., Huang, B., Zhang, B., Xiang, Y., Du, Z., Xu, Q., Li, Y., Wang, Q., Ma, J., Peng, X., et al. (2016). Resetting epigenetic memory by reprogramming of histone modifications in mammals. Mol. Cell *63*, 1066–1079.

STAR★METHODS

KEY RESOURCES TABLE

REAGENT or RESOURCE	SOURCE	IDENTIFIER
Antibodies		
H3K27ac antibody	Active Motif	Cat # 39133; RRID:AB_2561016
H3K9me3 antibody	Abcam	Cat # ab8898; RRID:AB_306848
SMC3 antibody	Abcam	Cat # ab9263; RRID:AB_307122
Biological Samples		
MEF donor cells	This study	N/A
Cumulus cell donor cells	This study	N/A
Differentiated SCC1-AID mESC donor cells	This study	N/A
SCNT Embryos	This study	N/A
Chemicals, Peptides, and Recombinant Proteins		
pregnant mare serum gonadotropin (PMSG)	Ningbo Hormone Product Co., Ltd., China	Cat # 110254564
human chorionic gonadotropin (HCG)	Ningbo Hormone Product Co., Ltd., China	Cat # 110251283
0.25% trypsin/EDTA	GIBCO	Cat # 2530-0-056
DMEM	GIBCO	Cat # 11965-092
Fetal bovine serum	Fetuin	Cat # 341506
Hyaluronidase	Sigma	Cat # H3506
MEM Non-Essential Amino Acids Solution	GIBCO	Cat # 111040050
GlutaMAX Supplement	GIBCO	Cat # 35050061
2-mercaptoethanol	Millipore	Cat # ES-007-E
EmbryoMax 100X nucleosides	Millipore	Cat # ES-008-D
LIF	Millipore	Cat # ESG1107
Auxin	Sigma	Cat # 6505-45-9
SrCl$_2$	Sigma	Cat # 255521
cytochalasin B	Sigma	Cat # C-6762
G1-Plus medium	Vitrolife	Cat # 10132
acid Tyrode's solution	Sigma	Cat # T-1788
Biotin-14-dCTP	Thermo Fisher	Cat # 19518018
MboI	New England Biolabs	Cat # R0147M
T4 DNA ligase	New England Biolabs	Cat # M0202L
T4 DNA Polymerase	New England Biolabs	Cat # M0203L
T4 Polynucleotide Kinase	New England Biolabs	Cat # M0201L
Klenow Fragment (3′→5′ exo-)	New England Biolabs	Cat # M0212L
DNA Polymerase I, Large (Klenow) Fragment	New England Biolabs	Cat # M0210L
Proteinase K	Roche	Cat # 10910000
DAPI	Invitrogen	Cat # D1306
AMPure XP beads	Beckman Coulter	Cat # A63881
Dynabeads MyOne Streptavidin C1 beads	Thermo Fisher	Cat # 65001
DNA suspension Buffer	TEKnova	Cat # PNT0221
Mineral oil	Signa-Aldrich	Cat # M8410
Halt^{TM} Protease Inhibitor Cocktail	Thermo Scientific	Cat # 78430
BSA	New England Biolabs	Cat # B9000S
hypotonic lysis buffer	Amresco	Cat # M334

(Continued on next page)

Continued

REAGENT or RESOURCE	SOURCE	IDENTIFIER
Concanavalin A beads	Polysciences	Cat # 86057
5% Digitonin	Thermo	Cat # BN2006
Phenylmethanesulfonyl fluoride (PMSF)	Sigma	Cat # 329-98-6
protein A/G Dynabeads	Life Technologies	Cat # 10015D
Retinoic acid	Sigma	Cat # R2625
poly-L-ornithine	Sigma	Cat # P3655
Laminin	Invitrogen	Cat # 23017-015
DMEM/F-12	GIBCO	Cat # 11330-032
B27	Life tech	Cat # 17504-044
BME	GIBCO	Cat # 21010-046
Critical Commercial Assays		
TruePrep DNA library preparation Kit	Vazyme	Cat # TD503-01
TruePrepTM Index Kit V2 for Illumina®	Vazyme	Cat # TD202/207
NEBNext Ultra II DNA Library Prep Kit for Illumina	New England Biolabs	Cat # E7645S
ChamQ Universal SYBR qPCR Matser Mix	Vazyme	Cat # Q711
Deposited Data		
Hi-C data from staged SCNT donor cells and reconstructed embryos	This Study	GEO: GSE139430
RNA-seq data from staged SCNT reconstructed embryos	This Study	GEO: GSE139430
Imaging Data (Mendeley)	This Study	https://dx.doi.org/10.17632/vyfpfvb2th.3
MEF Hi-C Datasets	Barutcu et al., 2018	GEO: GSE98632
Early embryo Hi-C Datasets	Du et al., 2017	GEO: GSE82185
Mouse cumulus cell-derived SCNT embryo RNA-Seq Datasets	Liu et al., 2018	GEO: GSE70608
SCNT Reprogramming resistant regions Datasets	Matoba et al., 2014	GEO: GSE59073
MEF CTCF Datasets	Gdula et al., 2019	GEO: GSE122019
mESC CTCF Datasets	Shen et al., 2012	GEO: GSE29184
mESC SMC3 Datasets	Kagey et al., 2010	GEO: GSE22557
Mouse fertilized embryo RNA-Seq Datasets	Zheng et al., 2016	GEO: GSE71434
Experimental Models: Cell Lines		
SCC1-AID mESC cell line	Rhodes et al., 2020	N/A
Experimental Models: Organisms/Strains		
C57BL/6N mice	Beijing Vital River Laboratory Animal Technology Co., Ltd.	Stock number 213
PWK/PhJ mice	Jackson Laboratory	Cat # 003715
B6D2F1(C57BL/6 × DBA/2) mice	This study	N/A
Oligonucleotides		
Zscan4-1 siRNA 5′-CCAGUCAUCAUGUAGACUUTT-3′	This study	N/A
Zscan4-2 siRNA 5′-GCCAGUAGACACCACACAATT-3′	This study	N/A
Zscan4-3 siRNA 5′-CCAGAGAACUCACCUGAAUTT-3′	This study	N/A
Scrambled siRNA 5′-UUCUCCGAACGUGUCACGUTT-3′	This study	N/A
Zscan4 qPCR primer forward-5′-GAGATTCATGGAGAG TCTGACTGATGAGTG-3′	Zalzman et al., 2010	N/A
Zscan4 qPCR primer reverse-5′-GCTGTTGTTTCAAAAG CTTGATGACTTC-3′	Zalzman et al., 2010	N/A

Continued

REAGENT or RESOURCE	SOURCE	IDENTIFIER
Zscan4c qPCR primers forward-5′-CCGGAGAAAGCAG TGAGGTGGA-3′	Zalzman et al., 2010	N/A
Zscan4c qPCR primers reverse-5′-CGAAAATGCTAAC AGTTGAT-3	Zalzman et al., 2010	N/A
Zscan4d qPCR primers forward-5′-GTCCTGACAGAG GCCTGCC-3′	Zalzman et al., 2010	N/A
Zscan4d qPCR primers reverse-5′-GAGATGTCTGAAGA GGCAAT-3′	Zalzman et al., 2010	N/A
Gapdh qPCR primers forward-5′-TTCACCACCATGGAG AAGGC-3′	Ishiguro et al., 2017	N/A
Gapdh qPCR primers reverse-5′- GGCATGGACTGTGG TCATGA-3′	Ishiguro et al., 2017	N/A
Zfp352 qPCR primers forward-5′-AAAGCCTTGATCCTC AGGTG-3′	Hendrickson et al., 2017	N/A
Zfp352 qPCR primers reverse-5′-GCCGAAGAGTTTTTC TGAGG-3′	Hendrickson et al., 2017	N/A
Usp17la qPCR primers forward-5′- TTTGTAGACACGG TGGTTGC-3′	Hendrickson et al., 2017	N/A
Usp17la qPCR primers reverse-5′- GGGAGCAGAAGG AAGTTTTTC-3′	Hendrickson et al., 2017	N/A
Software and Algorithms		
Bowtie2 (v2.2.6)	Langmead and Salzberg, 2012	http://bowtie-bio.sourceforge.net/bowtie2/index.shtml
HiC-Pro (v2.7.1b)	Servant et al., 2015	https://github.com/nservant/HiC-Pro
BEDtools	Quinlan and Hall, 2010	https://bedtools.readthedocs.io/en/latest/
SAMtools	Li et al., 2009	https://github.com/samtools/samtools
R package: ape	Paradis et al., 2004	https://cran.r-project.org/web/packages/ape/index.html
R package: preprocessCore	Bolstad et al., 2003	https://github.com/bmbolstad/preprocessCore
Java TreeView	Saldanha, 2004	http://jtreeview.sourceforge.net/
C-world (Hi-C analysis software)	Job Dekker lab	https://github.com/dekkerlab/cworld-dekker
HiCPlotter (v0.6.05.compare)	Akdemir and Chin, 2015	https://github.com/kcakdemir/HiCPlotter
TopHat (version 2.0.11)	Kim et al., 2013	https://ccb.jhu.edu/software/tophat/index.shtml
Cufflinks (version 2.0.2)	Trapnell et al., 2012	http://cole-trapnell-lab.github.io/cufflinks
Cluster	de Hoon et al., 2004	http://bonsai.hgc.jp/~mdehoon/software/cluster/index.html
MACS2 (version 2.2.6)	Zhang et al., 2008	https://github.com/macs3-project/MACS
GenomeDISCO	Ursu et al., 2018; Yardımcı et al., 2019	https://github.com/kundajelab/genomedisco
deepTools	Ramírez et al., 2016	https://deeptools.readthedocs.io/en/develop/content/example_usage.html

RESOURCE AVAILABILITY

Lead Contact

Further information and requests for resources and reagents should be directed to and will be fulfilled by the lead contact, Wei Xie (xiewei121@tsinghua.edu.cn).

Materials Availability

This study did not generate new unique reagents. All the reagents used in this study are available from the Lead Contact with a completed Materials Transfer Agreement.

Data and Code Availability

The data generated during this study have been deposited in the NCBI Gene Expression Omnibus (GEO) with the accession number GEO: GSE139430.

Public data analyses for MEF Hi-C datasets, mouse embryo sisHi-C datasets, mouse fertilized embryo RNA-seq datasets, mouse cumulus cell-derived SCNT embryo RNA-seq datasets, SCNT reprogramming resistant regions datasets, MEF CTCF binding datasets, mESC CTCF binding datasets and mESC SMC3 binding datasets were downloaded from NCBI Gene Expression Omnibus with the accession numbers GEO:GSE98632,GEO: GSE82185, GEO: GSE71434, GEO:GSE70608, GEO:GSE59073, GEO:GSE122019, GEO:GSE29184 and GEO:GSE22557 respectively.

Original microscopic images in this study have been deposited in the Mendeley Data (https://dx.doi.org/10.17632/vyfpfvb2th.3). All other data supporting the findings of this study are available from the Lead Contact on reasonable request.

EXPERIMENTAL MODEL AND SUBJECT DETAILS

Animals

All mice were housed in a temperature-controlled environment under a 12 hours light: 12 hours dark cycle. All animal procedures complied with the Animal Care and Use Committee of Huazhong Agriculture University (HZAUMO-2016-031). 8–10 weeks old female B6D2F1 (C57BL/6 × DBA/2) mice were used as the recipient mice for SCNT. Metaphase II (MII) stage oocytes were collected from super-ovulated mice by intraperitoneal injection with pregnant mare serum gonadotropin (PMSG) (Ningbo Hormone Product Co., Ltd., China) and followed with human chorionic gonadotropin (HCG) (Ningbo Hormone Product Co., Ltd., China) injection after 48 hours. C57BL/6N (female) and PWK/PhJ (male) strain mice were used for mouse embryonic fibroblasts (MEFs) derivation. B6D2F1 strain mice were used for cumulus cell derivation.

Cell lines

SCC1-AID-mESC cell line was generously provided by Dr. Robert Klose (Rhodes et al., 2020). The mESCs were cultured in DMEM supplemented with 10% Fetal Bovine Serum (FBS), MEM Non-Essential Amino Acids Solution (GIBCO, Cat # 111040050), GlutaMAX Supplement (GIBCO, Cat # 35050061), 2-mercaptoethanol (Millipore, Cat # ES-007-E), EmbryoMax 100X nucleosides (Millipore, Cat # ES-008-D), LIF (1000 U/ml, Millipore, Cat # ESG1107).

Primary cell culture

MEF cells were derived from male mouse embryos at 13.5 dpc, obtained from C57BL/6N (female) mating with PWK/PhJ (male). Embryos were processed by removing heads, limbs and internal organs, washing and cutting into smaller pieces in tubes, trypsinizing with 0.25% trypsin/EDTA (GIBCO, Cat # 2530-0-056). The mixture of tissues was filtered and centrifuged at 2,000 rpm for five minutes. The supernatant was removed, the cell pellets were resuspended with DMEM (GIBCO, Cat # 11965-092) supplemented with 10% fetal bovine serum (FBS) (Fetuin, Cat # 341506) in the 100 mm Petri dish culture at 37°C, 5% CO2 incubator. Cumulus cells were collected from cumulus-oocyte complexes of BDF1 female mouse, which was digested by hyaluronidase (Sigma, Cat # H3506).

METHOD DETAILS

Donor cell preparation

Male MEF cells, cumulus cells and SCC1-AID differentiated cells were used as SCNT nuclear donor cells. For differentiation, mESCs were cultured in medium without LIF for 3 days and treated without/with Auxin (500 μM) (Sigma, Cat # 6505-45-9) for 1 day. SCC1-AID differentiated cells were dissociated into single cells. Sorting was then conducted using FACS Jazz (BD Biosciences) to remove all the dead cells. GFP fluorescence signals were examined to confirm the SCC1 depletion efficiency. Cells in auxin treatment group were collected as SCC1- groups, while the differentiated cells without the auxin treatment were collected as SCC1+ groups.

Nuclear transfer

SCNT was performed as previously described (Gao et al., 2003). Briefly, MII oocytes were obtain at 13-14 hours after HCG injection. The spindle of oocyte was removed by the Piezo-driven (PrimeTech, Osaka, Japan) enucleation pipette on the Olympus inverted microscope (Tokyo, Japan), and the nuclei of donor cells were directly injected into the enucleated oocytes. The reconstructed oocytes were incubated in CZB medium for 1 hour before activation treatment. The cloned constructs were activated in Ca^{2+}-free CZB medium supplemented with 10 mM SrCl$_2$ (Sigma, Cat # 255521) and 5 μg/ml of cytochalasin B (Sigma, Cat # C-6762) for 4 hours. Cloned embryos were cultured in G1-Plus medium (Vitrolife, Cat # 10132) at 37.5°C in an atmosphere of 5% CO$_2$ in air. Each set of embryos at a particular stage was collected for experiment: reconstructed oocytes cultured in CZB medium for 1 hour (PCC), and various time after activation including 4 hours (PPN1), 6 hours (PPN3), 10 hours (PPN5) (with pronucleus selection), 28 hours (late 2-cell), and 56 hours (8-cell). The first polar body was removed by enucleation pipette on the micromanipulator, while the zona pellucida was gently removed by treatment with acid Tyrode's solution (Sigma, Cat # T-1788) for several minutes. The embryos were then manually picked and prepared for the further sisHi-C and RNA-seq experiments.

Knockdown of Zscan4 in cloned embryos

Three mouse *Zscan4* siRNA and one scrambled siRNA were synthesized for the *Zscan4* knock-down experiments. The siRNA oligonucleotides sequence information is as the following: *Zscan4*-1: 5′-CCAGUCAUCAUGUAGACUUTT-3′ (sense), *Zscan*4-2: 5′-GCCAGUAGACACCCACACAATT-3′ (sense); *Zscan4*-3: 5′-CCAGAGAACUCACCUGAAUTT-3′ (sense); Scrambled siRNA: 5′-UU CUCCGAACGUGUCACGUTT-3′ (sense). Each mouse *Zscan4* siRNA or scrambled siRNA was diluted in nuclease-free water to a final concentration of 50 μM. The MII oocytes were injected with 50 μM *Zscan4* siRNA (three *Zscan4* siRNA combined) or scrambled siRNA using a Piezo-driven micromanipulator. After incubation for 30mins in CZB medium, these oocytes were enucleated and further subjected to SCNT (Liu et al., 2016). The knock-down efficiency was then validated at the SCNT late 2-cell stage. Briefly, embryos were lysed in hypotonic lysis buffer (Amresco, Cat # M334), and the polyadenylated mRNAs were captured by the Oligo(dT) primers. After ~3–10 mins lysis at 72 °C, the Smart-seq2 reverse transcription reactions were performed. After pre-amplification and AMPure XP beads purification, cDNAs were quantitatively analyzed for the relative abundance of *Zscan4*, *Zscan4c*, *Zscan4d*, *Usp17la*, *Zfp352* and *Gapdh* using ChamQ Universal SYBR qPCR Matser Mix (Vazyme, Cat #Q711). The RT-PCR primers for the related genes were based on previous publications (Hendrickson et al., 2017; Ishiguro et al., 2017; Zalzman et al., 2010). *Zscan4*: forward-5′-GAGATTCATGGAGAGTCTGACTGATGAGTG-3′, reverse-5′-GCTGTTGTTTCAAAAGCTTGATGACTTC-3′; *Zscan4c*: forward-5′-CCGGAGAAAGCAGTGAGGTGGA-3′, reverse-5′-CGAAAATGCTAACAGTTGAT-3′; *Zscan4d*: forward-5′-GTCCTGACA GAGGCCTGCC-3′, reverse-5′-GAGATGTCTGAAGAGGCAAT-3′; *Usp17la*: forward-5′-TTTGTAGACACGGTGGTTGC-3′, reverse-5′- GGGAGCAGAAGGAAGTTTTTC-3′; Zfp352: forward-5′-AAAGCCTTGATCCTCAGGTG-3′, reverse-5′-GCCGAAGAGTTTTTCT GAGG-3′; *Gapdh*: forward-5′-TTCACCACCATGGAGAAGGC-3′, reverse-5′- GGCATGGACTGTGGTCATGA-3′. *Gapdh* was used as the internal control, the relative abundance of *Zscan4*, *Zscan4c*, *Zscan4d*, *Usp17la* and *Zfp352* was calculated using the $2^{-\Delta\Delta CT}$ method.

Neuron differentiation

SCC1-AID mES cells were subjected to neuron differentiation as previously described (Zhang et al., 2016). Briefly, mES cells were cultured in non-adhesive bacterial dishes using ES culture medium minus LIF for four days. Retinoic acid (RA) (Sigma, Cat. R2625) was then added to medium to a final concentration of 2 μg/ml. On the fifth day after adding RA, embryonic bodies were dissociated by 0.25% Trypsin-EDTA (GIBCO, Cat. 25200-056) and plated to poly-L-ornithine (Sigma, Cat. P3655) and Laminin (Invitrogen, Cat. 23017-015) pre-coated dish. Cells were cultured in DMEM/F-12 (GIBCO, Cat. 11330-032) with B27 (Life tech., Cat. 17504-044) and were incubated for two days. The medium was switched to BME (GIBCO, Cat. 21010-046) with B27 for another two days. Differentiated neurons were then subjected to the auxin treatment and harvested for subsequent analyses.

DAPI staining

Embryos were fixed in 4% paraformaldehyde overnight in 4°C. DNA was labeled by DAPI (Invitrogen, Cat # D1306). Stained embryos mounted on slides were observed using a fluorescence microscope.

Immunostaining

For cell lines, the cells were first mounted on the glass slides during cell culture. For embryos, the embryos were first treated with acidic Tyrode's solution to remove zona pellucida. Samples were then fixed in 4% PFA for 1 hour at room temperature, permeabilized with 0.5% Triton X-100 in PBS at room temperature for 30 mins and blocked with 0.1% BSA in PBS at room temperature for 1 hour. Samples were incubated with the H3K27ac antibody (Active motif, Cat # 39133, RRID:AB_2561016,1:500) at 4°C overnight. Samples were washed with PBST (PBS with 0.1% Triton X-100) three times and incubated with secondary antibodies (Alexa fluor 594 goat anti-rabbit, 1:400) for 1 hour at room temperature. DNA was stained with DAPI. After staining, embryos were mounted on glass slides in PBS. Images were acquired on a Zeiss 780 or Zeiss 880 confocal microscope. The same parameters were used for individual channel of all groups of samples. The fluorescence intensity of H3K27ac and DAPI was quantified using Fiji software.

sisHi-C library generation and sequencing

The sisHi-C library generation was performed as described previously (Du et al., 2017). Briefly, cells were fixed with 1% formaldehyde at room temperature (RT) for 10 mins. Formaldehyde was quenched with glycine for 10 mins at RT. Cells were washed with 1XPBS for two times and then lysed in 50 μl lysis buffer (10 mM Tris-HCl pH7.4, 10 mM NaCl, 0.1 mM EDTA, 0.5% NP-40 and proteinase inhibitor) on ice for 50 mins. After spinning at 3000 rpm/min in 4°C for 5 mins, the supernatant was discarded with a pipette carefully. Chromatin was solubilized in 0.5% SDS and incubated at 62°C for 10 mins. SDS was quenched by 10% Triton X-100 at 37°C for 30 mins. Then the nuclei were digested with 50 U MboI at 37°C overnight with rotation. MboI was then inactivated at 62°C for 20 minutes. To fill in the biotin to the DNA, dATP, dGTP, dTTP, biotin-14-dCTP and Klenow were added to the solution and the reaction was carried out at 37°C for 1.5 hours with rotation. The fragments were ligated at RT for 6 hours with rotation. This was followed by reversal of crosslink and DNA purification. DNA was sheared to 300-500 bp with Covaris M220. The biotin-labeled DNA was then pulled down with 10 μl Dynabeads MyOne Streptavidin C1 (Life Technology). Sequencing library preparation was performed on beads, including end-repair, dATP tailing and adaptor-ligation. DNA was eluted twice by adding 20 μl water to the tube and incubation at 66°C for

20 minutes. 9-15 cycles of PCR amplification were performed with Extaq (Takara). Finally, size selection was done with AMPure XP beads and fragments ranging from 200 bp to 1000 bp were selected. All the libraries were sequenced on Illumina HiSeq2500 or HiSeq XTen according to the manufacturer's instruction.

RNA-seq library preparation and sequencing

The RNA-seq libraries were generated using the Smart-seq2 protocol as described previously with minor modification (Picelli et al., 2014). Briefly, cells or embryos were lysed in hypotonic lysis buffer (Amresco, Cat # M334), and the polyadenylated mRNAs were captured by the Oligo(dT) primers. After ~3–10 mins lysis at 72 °C, the Smart-seq2 reverse transcription reactions were performed. After pre-amplification and AMPure XP beads purification, cDNAs were subject to Vazyme TruePrep DNA library preparation (Vazyme, Cat # TD503-01 and Cat # TD202/207). All libraries were sequenced on Illumina HiSeq 2500 or HiSeq XTen according to the manufacturer's instruction.

ChIP-seq library generation and sequencing

H3K27ac and H3K9me3 ChIP-seq in mESCs was performed as previously described (Brind'Amour et al., 2015). Briefly, mESCs were re-suspended in nuclear isolation buffer (Sigma). Depending on input size chromatin was fragmented for 5–7.5 mins using MNase at 21 or 37 °C, and diluted in NChIP immunoprecipitation buffer (20 mM Tris-HCl pH 8.0, 2 mM EDTA, 15 mM NaCl, 0.1% Triton X-100, 1 × EDTA-free protease inhibitor cocktail and 1 mM phenylmethanesulfonyl fluoride (Sigma, Cat # 329-98-6)). Chromatin was pre-cleared with 5 or 10 μl of 1:1 protein A/G Dynabeads (Life Technologies, Cat # 10015D) and then incubated with antibody (H3K9me3, Abcam, Cat # ab8898, RRID:AB_306848; H3K27ac, Active Motif, Cat # 39133, RRID:AB_2561016) overnight at 4 °C. Next, complexes were washed twice with 400 μl of ChIP wash buffer I (20 mM Tris-HCl, pH 8.0, 0.1% SDS, 1% Triton X-100, 0.1% deoxycholate, 2 mM EDTA and 150 mM NaCl) and twice with 400 μl of ChIP wash buffer II (20 mM Tris-HCl (pH 8.0), 0.1% SDS, 1% Triton X-100, 0.1%deoxycholate, 2 mM EDTA and 500 mM NaCl). Protein–DNA complexes were eluted in 30 μl of ChIP elution buffer (100 mM NaHCO$_3$ and 1% SDS) for 1.5 hours at 68 °C. DNA was purified by phenol chloroform and ethanol-precipitated. Purified DNA was subjected to Tru-seq library construction using NEBNext Ultra II DNA Library Prep Kit for Illumina (NEB, E7645S). The products were purified and size-selected with AMPure XP beads (Beckman Coulter, Cat # A63881).

CUT&RUN library generation and sequencing

SMC3 CUT&RUN in mESCs was conducted as previously described (Skene and Henikoff, 2017). Briefly, samples were resuspended by washing buffer (HEPES-KOH, pH = 7.5, 20 mM; NaCl, 150 mM; Spermidine, 0.5 mM and with Roche complete protease inhibitor) and incubated with concanavalin-coated magnetic beads (Polyscience, 86057) at 23°C for 10 mins. Next, the samples were resuspended by antibody buffer (washing buffer plus digitonin (Thermo, Cat # BN2006), freshly pre-heated, 0.005%~0.01%, tested for each batch; EDTA, pH = 8.0, 2 mM) with SMC3 antibody (Abcam, Cat #ab9263, RRID:AB_307122) diluted at ratio of 1:100. After being incubated at 4°C for overnight, the samples were resuspended by washing buffer with pA-MNase (to a final concentration of 700ng/mL) and incubated at 4°C for 3 hours. The targeted digestion was then performed with CaCl$_2$ treatment and quenched by stop buffer. Purified DNA was subjected to Tru-seq library construction using NEBNext Ultra II DNA Library Prep Kit for Illumina (NEB, E7645S). The products were purified and size-selected with AMPure XP beads (Beckman Coulter, Cat # A63881).

Data analysis

Hi-C data processing

Paired end raw reads of Hi-C libraries were aligned, processed and iteratively corrected using HiC-Pro (version 2.7.1b) as described (Servant et al., 2015). Briefly, sequencing reads were first independently aligned to the mouse reference genome (mm9) using the bowtie2 end-to-end algorithm and "-very-sensitive" option. To rescue the chimeric fragments spanning the ligation junction, the ligation site was detected and the 5′ fraction of the reads was aligned back to the reference genome. Unmapped reads, multiple mapped reads and singletons were then discarded. Pairs of aligned reads were then assigned to MboI restriction fragments. Read pairs from uncut DNA, self-circle ligation and PCR artifacts were filtered out and the valid read pairs involving two different restriction fragments were used to build the contact matrix. Valid read pairs were then binned at a specific resolution by dividing the genome into bins of equal size. We chose 100-kb bin size for examination of global interaction patterns of the whole chromosome, and 40-kb bin size to show local interactions and to perform TAD calling. The binned interaction matrices were then normalized using the iterative correction method (Imakaev et al., 2012; Servant et al., 2015) to correct the biases such as GC content, mappability and effective fragment length in Hi-C data.

RNA-seq data processing

All RNA-seq data were mapped to mouse reference genome (mm9) by TopHat (version 2.0.11) (Kim et al., 2013). The gene expression level was calculated by Cufflinks (version 2.0.2) (Trapnell et al., 2012) using the refFlat database from the UCSC genome browser. Only uniquely mapped reads were kept for further analysis. The gene expression levels for mouse fertilized embryos and the SCNT embryos derived from cumulus cells are from the published RNA-seq datasets (Liu et al., 2018). To identify the differentially expressed genes among different samples, FPKM value calculated by Cufflinks for each sample is further quantile-normalized using the R package (preprocessCore) (Bolstad et al., 2003).

ChIP-seq data processing

The paired-end ChIP reads were aligned with the parameters: -t –q –N 1 –L 25 –X 1000–no-mixed–no-discordant to mm9 reference genome by Bowtie2 (version 2.2.6) (Langmead and Salzberg, 2012). All unmapped reads, reads with low mapping quality (MAPQ < 20) and PCR duplicates were removed. For downstream analysis, we normalized the read counts by computing the numbers of reads per kilobase of bin per million of reads sequenced (RPKM) for 100-bp bins of the genome. To minimize the batch and cell type variation, RPKM values across whole genome were further Z-score normalized. Z-score normalization was obtained using the following formula: for a given promoter i: $z_i = (x_i - \mu)/\sigma$, where x_i is the RPKM value before normalization, z_i is the normalized RPKM value and μ and σ are the mean and standard deviation of all promoter RPKM values for each stage, respectively. To visualize the ChIP signals in the UCSC genome browser, we generated the RPKM values on a 100bp-window base.

CUT&RUN data processing

As described previously (Xia et al., 2019), the pair-end CUT&RUN reads were aligned to mm9 reference genome with random chromosome cleaned by Bowtie2 (version 2.2.6) (Langmead and Salzberg, 2012) under the parameters –t –q –N 1 –L 25. All unmapped reads, reads with low mapping quality (MAPQ < 20) and PCR duplicates were removed. For downstream analysis, we normalized the read counts by computing the numbers of reads per kilobase of bin per million of reads sequenced (RPKM) for 100-bp bins of the genome using the SAMtools (Li et al., 2009), BEDtools (Quinlan and Hall, 2010) and deepTools (Ramírez et al., 2016) softwares. To minimize the batch and cell type variation, RPKM values across whole genome were further Z-score normalized. Z-score normalization was obtained using the following formula: for a given promoter i: $z_i = (x_i - \mu)/\sigma$, where x_i is the RPKM value before normalization, z_i is the normalized RPKM value and μ and σ are the mean and standard deviation of all promoter RPKM values for each stage, respectively. To visualize the CUT&RUN signals in the UCSC genome browser, we generated the RPKM values on a 100bp-window base.

Analysis of the histone mark or cohesin enrichment

The transcription start sites (TSSs) information of the minor ZGA genes were identified using the refFlat database from the UCSC genome browser. The histone mark or cohesin enrichment at promoter regions (+/− 2.5kb from TSSs) was computed using Z-score normalized RPKM. In the cohesin enrichment analysis, the cohein enrichment at mESC CTCF binding sites (Gdula et al., 2019; Shen et al., 2012) was used as the positive control.

Reproducibility of sisHi-C data

The reproducibility of sisHi-C data was assessed using GenomeDISCO (Ursu et al., 2018; Yardımcı et al., 2019). Paired end raw reads of Hi-C libraries were aligned, processed and iteratively corrected using HiC-Pro (version 2.7.1b) as described (Servant et al., 2015). The raw interaction matrices within the resolution of 500-kb bins were further smoothed by random walks (steps parameter t = 3). Next, the differences between denoised contact matrices were computed and converted into a concordance score. The genome-wide reproducibility score is the average of the scores across all chromosomes.

Hi-C interaction heatmap, differential interaction heatmap, and correlation heatmap

All the Hi-C interaction frequency heatmaps of whole chromosomes and the zoom-in views were generated using HiCPlotter version 0.6.05.compare, a Hi-C data visualization tool (Akdemir and Chin, 2015). To generate the correlation heatmap, the correlation matrices for each stage were generated as previously described (Lieberman-Aiden et al., 2009). The heatmap was then generated with Java TreeView (Saldanha, 2004).

Analysis of inter-chromosomal read pairs

For each pair of different chromosomes (chromosomes 1–2, 1–3, 1–4 and so on), the numbers of read pairs were counted and then divided by the total read-pairs. Boxplots were used to show the distribution of the ratios for all pairs of chromosomes.

Contact decay curve

Contact decay curve was calculated as previously described (Nagano et al., 2017). Briefly, we used normalized valid-pairs, and only the intra-chromosomal interaction beyond 20kb are kept. We first divided interaction distances between two regions into logarithmically spaced bins with increasing factor $2^{0.125}$ (20kb, 20kb × $2^{0.125}$, 20kb × $2^{0.25}$ …) as previously described (Nagano et al., 2017). Next, for each bin, we counted the number of interactions at corresponding distances. The probability of contact was calculated by dividing the number of interactions in each bin by the total number of interactions among all the bins.

Analysis of topologically associating domains (TADs)

40-kb resolution sisHi-C matrices were used for TAD boundaries identification by calculating the insulation score of each bin as previously described (Crane et al., 2015). Briefly, the insulation score was calculated by sliding a 1Mb X 1Mb square along the diagonal of the interaction matrix for every chromosome. A 200-kb window was used for calculation of the delta vector. Boundaries with a "boundary strength" less than 0.25 were removed. The average insulation scores were plotted around all TADs as well as their nearby regions (+/− 0.5 TAD length).

Average interaction heatmap of TADs

We used all TADs in MEFs as representatives of mature TADs, and plotted the composite interaction frequency by averaging all TADs along early development. The locations of MEF TAD boundary were confirmed using published dataset (Barutcu et al., 2018). The resulted matrices were then normalized by the average levels of the matrix values to make the sum of matrices for different stages equal. To generate the differential heatmap for average interactions of TADs, interaction matrices of the first stage were subtracted from the second stage. In the differential matrices, positive values indicate that the interaction frequency at the second stage is higher than that at the first stage, and vice versa.

Consolidation score

We used a TAD consolidation score to quantify the states of TADs as previously described (Du et al., 2017). Briefly, the score is defined as the ratio of average interaction frequency within each TAD (excluding short-distance interactions < 400 kb) and the local background interaction frequency from nearby non-TAD regions. High scores indicate strong consolidation of TADs.

Identification of chromatin compartments

A and B compartments were identified as previously described with some modifications. The normalized 100 kb and 300kb interaction matrices for each stage were used in this analysis. First, the bins that have no interactions with any other bins were removed before expected interaction matrices were calculated. Observed/Expected matrices were generated using a sliding window approach (Dixon et al., 2015) with the bin size of 600 kb and the step size of 300 kb for 300-kb resolution, while a bin size of 400kb and a step size of 100kb were used for the 100-kb resolution analysis. Principal component analysis was performed on the correlation matrices generated from the observed/expected matrices. The first principal component of the correlation matrices were used to identify A/B compartments. Gene density of the whole chromosome was used to correct if A/B calling was inverted for the entire chromosome (no correction was done for individual regions). The regions in which PC1 values >0.005 are classified into A compartments, while the regions in which PC1 values <-0.005 are identified into B compartments.

Clustering analysis

The k-means clustering of gene expression level or PC1 values at various stages was conducted using Cluster 3.0 (de Hoon et al., 2004)with the parameters -g 7 (Euclidean distance). Heatmaps were generated using Java Treeview (Saldanha, 2004). The hierarchical clustering analysis based on the PC1 values at various stages was conducted using an R package (ape) (Paradis et al., 2004) based on the Pearson correlation as indicated between each pair of datasets. The distance between two datasets was calculated by (1 − correlation).

Analysis of compartment segregation using inter-compartment interactions

To compute the inter-compartment interactions between the same classes or different classes, we first removed local interactions that were shorter than 2Mb, which mainly reflect interactions within TADs rather than long-distance interactions between compartments. The remaining interactions were assigned to two categories: interactions between two bins located in the same class of compartments (including A–A interactions and B–B interactions) and interactions between two bins located in different classes of compartments (A–B interactions). Both the compartments defined in MEF and mESC were considered as mature compartments and their positions were used for all stages in this analysis. For each stage, the average interaction frequency between a pair of bins was calculated for each of the two categories for each chromosome. Next, the ratios between the average interaction frequency per a pair of A–A or B–B interactions and per a pair of A–B interactions were calculated for each chromosome. Boxplots were used to show the ranges of such ratios for all chromosomes (chr14 and X chromosome excluded) and to measure the degree of compartment segregation for each stage. Statistical analyses were implemented with R. *P value*s calculated by Wilcoxon rank-sum test (two-tailed).

Analysis of compartment classes

To classify compartment groups during fertilized and SCNT embryo development, we first identified the compartment A/B in donor cell, fertilized 8-cell and relative SCNT 8-cell embryos, according to their first principal component of the correlation matrices. Next, we defined "Static compartments" as those that remain A or B in all three cell types; "Reprogrammed compartments" refer to those that are A in donor cells, but become B (or vice versa) in both fertilized and SCNT 8-cell samples; "Resistant compartments" refer to those that switch compartments in fertilized embryos but fail to do so in SCNT embryos. We only used those that were classified into the same category in both two replicates for downstream analyses. To analyze the relationship between dynamic compartments and gene expression, we used quantile normalized RNA-seq dataset for donor cell, fertilized 8-cell and relative SCNT 8-cell embryos. We then mapped the RNA-seq data to each class of dynamic compartments. Only the genes which are expressed in at least one cell type were kept. Boxplots were used to show the ranges of gene expression levels in each group. Functional annotation of enrichment analysis was performed with DAVID.

Analysis of TAD boundary strength (TBS)

TAD boundaries were first identified in MEF and mESCs (to represent embryos), for which high-depth Hi-C data were available (Du et al., 2017), and then pooled. To further refine the boundary positions, we identified CTCF sites within these boundary bins (40kb-bin). To do so, CTCF binding sites within MEF or mESCs (Gdula et al., 2019; Shen et al., 2012) were first identified by MACS2 (Zhang et al., 2008) and only the strong peaks (average normalized RPKM > 3) within these two cell types were then pooled. We then defined "TAD Boundary Strength" (TBS) as the Hi-C insulation score differences between these CTCF binding site and its neighbor regions (+/− 120kb, 3 bins in Hi-C data matrix). The TBS scores at these identified CTCF binding sites for each stage were further used for normalization (Z-score). Next, we selected dynamic TAD boundaries with significantly different TBS scores between fertilized 8-cell and MEF ($TBS_{(MEF)}$-$TBS_{(Fertilized)}$ > 0.7 or < −0.7), and further required the TAD boundary to be lost in one of the cell types ($TBS_{(MEF)}$*$TBS_{(Fertilized)}$ < 0). The rest boundaries were considered as "Static." Next, if $TBS_{(SCNT)}$ is closer to $TBS_{(Fertilized)}$ (($TBS_{(SCNT)}$-$TBS_{(MEF)}$)/($TBS_{(Fertilized)}$-$TBS_{(MEF)}$) > 0.75), we classified this TAD boundary as "Reprogrammed" in SCNT embryos. Otherwise if it is closer to $TBS_{(MEF)}$ (($TBS_{(SCNT)}$-$TBS_{(MEF)}$)/($TBS_{(Fertilized)}$-$TBS_{(MEF)}$) < 0.25), it would be classified into "Resistant" group. The rest dynamic TAD boundaries were classified into "Intermediate" group. To analyze the relationship between dynamic TAD boundaries and gene expression, we used quantile normalized RNA-seq datasets from donor cell, fertilized 8-cell and SCNT

8-cell embryos. We first identified differentially expressed genes (DEGs) (fold change > 5; either SCNT or fertilized 8-cell embryos show minimal FPKM of 5). TAD boundaries residing within 1Mb of DEGs were counted as "near DEGs." Functional annotation of enrichment analysis was performed with DAVID.

QUANTIFICATION AND STATISTICAL ANALYSIS

The number of n biological replicates is provided within each figure legend. Statistical p values were calculated using two-tailed Wilcoxon rank-sum test in interaction frequency results. Statistical p values were calculated using two-tailed t test in gene expression level results. The error bars denote SEM, and the center values denote mean.